MICROSTRUCTURAL CHARACTERISATION OF SUBSURFACE DEFORMATION AND THE DEGRADATION OF STELLITE 6 INDUCED BY SELF-MATED SLIDING CONTACT IN A SIMULATED PWR ENVIRONMENT

M.J. Carrington[a] J.L. Daure[a] V.L. Ratia[a] D. Zhang[a] P.H. Shipway[a]

D.A. Stewart[b] D.G. McCartney[a]

[a] Advanced Materials Group, Faculty of Engineering, University of Nottingham, Nottingham, NG7 2RD, UK

[b] Rolls-Royce plc, UK

NOVEMBER 2020

HIGHLIGHTS

- Material removal via tribocorrosion increases significantly with temperature.
- The general mechanisms of degradation largely remain insensitive to temperature.
- Sliding contact generates an ϵ-martensite nanocrystalline subsurface microstructure.
- Plastic strain localisation is minimised and wear is confined to the nanoscale.

ABSTRACT

Stellite 6 (Co-29.5%Cr-5%W-1.2%C in wt%) is traditionally used as a hardfacing material in the primary circuit of pressurised water reactors (PWRs) due to its good corrosion and wear resistance in water at up to 300 ^{o}C. In this study, pin-on-disc type sliding contact tribocorrosion testing was conducted on HIPed Stellite 6 at 20 ^{o}C and 250 ^{o}C using a bespoke tribometer to simulate a primary circuit environment. Transmission electron microscopy (TEM), scanning electron microscopy (SEM), and X-ray diffraction (XRD) were used to characterize, for the first time, the material affected by tribocorrosion. Whilst the material loss increases by 16 - 39 times when the test temperature is increased from 20 ^{o}C to 250 ^{o}C; the mechanisms of degradation and deformation remain largely unchanged. Furthest from the sliding contact, strain is principally accommodated by the deformation-induced transformation of the γ Co-based matrix to ϵ-martensite. Closer to the sliding contact, the ϵ-martensite phase accommodates further strain via twinning and dislocation slip. At the sliding contact the intense deformation generates a nanocrystalline structure. The tribologically affected material is resistant to plastic strain localisation; this confines wear to the nanoscale where the synergistic effects of chemical degradation and mechanical deformation permit the removal of nanoscale particulates (corrosion enhanced nanowear (tribocorrosion)). The increased wear rate at 250 ^{o}C is attributed to a temperature dependent increase in corrosion enhanced nanowear. The degradation mechanisms revealed are important for the design of future hardfacings.

KEYWORDS

- Sliding Contact
- Hardfacing
- Tribocorrosion
- Transmission electron microscopy

1. INTRODUCTION

Hardfacing alloys are used to minimise tribological degradation of the surfaces of components subjected to sliding contact in the primary circuits of pressurised water reactors (PWRs). Primary circuits use lithiated water at 200 to 300 ^{o}C and within this aggressive environment, a number of critical components including valves, bearings, pumps (reactor coolant pumps), and control element drive mechanisms are exposed to degradation by the combined effects of loaded sliding contact and corrosion (tribocorrosion). The Co-based Stellite^{TM} family of hardfacing alloys (Co-Cr-Si-W-C type alloys) are used extensively because of their excellent performance in minimising both wear and corrosion. However, when ^{59}Co-based wear debris circulates through the reactor core, neutron bombardment permits nuclear activation and ^{59}Co is transmuted to the γ-emitting isotope ^{60}Co which has both a high and long-lived nuclear activity (half-life: $\sim$ 5.3 years). This is a major source of radiation exposure for plant maintenance workers which needs to be reduced and is a limitation on the continued use of Stellite hardfacings [1, 2].

Traditionally, hardfacing alloys have been applied to component substrate surfaces (typically 316 stainless steel) by techniques which are reliant upon solidification such as weld overlay or laser cladding where pores or cracks can readily form [3, 4]. However, due to the safety-critical nature and the long design lives required of the hardfaced components used in PWR applications, it is essential that the hardfacings are of high quality. Therefore, interest has grown in manufacturing hardfacing alloys by the consolidation of gas atomised powder using hot isostatic pressing (HIPing) and subsequently joining hardfacing inserts to substrate surfaces via a HIP-diffusion bonding process. Compared to traditional hardfacing processes, the powder HIP manufacturing route offers advantages which include better chemical and microstructural homogeneity and fewer defects [5].

This paper aims to comprehensively assess both the tribological and tribochemical performance of HIPed Stellite 6 during sliding in lithiated water at 20 ^{o}C and 250 ^{o}C. Despite the shortcomings of Stellite 6 when employed in a PWR environment, it has been found that its exceptional combination of wear and

corrosion resistance cannot be readily replicated in Co-free alloy systems such as the iron-based austenitic alloys NOREM [6] or Tristelle 5183 [7]. For these reasons, Stellite 6 is often regarded as the benchmark alloy against which the performance of other hardfacing alloys is assessed. However, a fundamental mechanistic understanding of why Stellite 6 exhibits such excellent tribological and tribochemical characteristics within a PWR environment remains somewhat fragmented and incomplete. The primary circuit operating environment of deoxygenated, lithiated water at up to 300 ^{o}C is known to play a critical role in the mechanisms of material loss, but there are relatively few reports available which comprehensively address this issue [8–14]. In broad terms, it is generally accepted that tribocorrosion is unquestionably significant to the degradation of Stellite 6 during sliding in lithiated water. However, there is a paucity of information in the literature concerning the mechanisms of tribocorrosion leading to material removal during the sliding of self-mated Stellite 6 in a PWR environment.

In light of the above, the degradation of Stellite 6 in a primary circuit PWR environment needs to be better understood. Tribocorrosion is known to be influenced by a combination of both complex mechanical and chemical phenomena [9, 15], so the main aim of the present work is to report the sub-surface nano-scale and micro-scale features of Stellite 6 following self-mated sliding contact in lithiated water. Accordingly, following pin-on-disc type wear tests conducted at 20 ^{o}C and 250 ^{o}C within a simulated primary circuit PWR environment, the tribologically affected material was investigated by a combination of X-ray diffraction, scanning electron microscopy and transmission electron microscopy, providing an understanding of the microstructural evolution of the contacting surface and the sub-surface as a result of sliding which is fundamental to understanding the mechanisms of tribocorrosion. Foundational to the development of new and improved cobalt-free alloys for future applications within PWRs is a better understanding of both the tribological and tribochemical performance of Stellite 6 and this work seeks to improve knowledge in this area.

2. Materials and Methods

2.1. Materials

Commercially available nitrogen gas atomised Stellite 6 powder was consolidated into bar form by HIPing and supplied by LSN Diffusion Ltd (Ammanford, SA18 3GY, UK). During the HIPing cycle the material was held at 1200 ^{o}C and 100 MPa for 4 h and cooled to room temperature. The chemical composition of HIPed Stellite 6 reported in (Table 1) was measured by AMG Analytical Services (Fullerton Road, Rotherham, S60 1D1, UK) and determined by inductively coupled plasma (ICP) spectrometry and Leco combustion analysis for the measurement of carbon and nitrogen. Samples for wear testing and metallurgical examination were machined from the HIPed bars using electrical discharge machining (EDM) and subsequently ground on the relevant faces to remove any recast layer associated with the EDM machining.

Table 1: Chemical composition of HIPed Stellite 6 as determined by chemical analysis.

	Element %							
	Co	**Cr**	**W**	**Si**	**C**	**Ni**	**Fe**	**Other**
wt%	Bal.	27.08	5.01	1.47	0.96	0.87	0.73	0.07
at%	Bal.	29.06	1.52	2.92	4.46	0.83	0.73	0.07

2.2. Sliding contact autoclave testing

Wear testing was conducted using a bespoke autoclave pin-on-disc tribometer which allowed testing to be conducted at 20 and 250 ^{o}C within an aqueous environment. The pin and discs were machined via EDM from the same HIPed material stock and the pin and disc test (contacting) surfaces were surface ground to an Ra of $\sim$ 0.4 μm. The cylindrical pins were machined to a 10 mm diameter and a 50 mm radius spherical end cap was ground onto the testing surface, whereas the discs were 30 mm in diameter with parallel ground end faces. The disc was

secured in a rotating sample holder and the pin was uniaxially loaded against the rotating disc through the application of a 4 kg dead load. This initial loading configuration generates a maximum Hertzian contact pressure of 0.372 GPa (elastic modulus: 237 GPa, Poisson ratio: 0.3 [16]). A free moving load stabilising mechanism prevented all lateral and rotational movement of the pin such that the pin and dead load assembly could only move in the direction normal to the plane defined by the test surface of the disc. The centre of the pin was loaded against the rotating disc at a position of 10 mm from the disc's axis of rotation; this resulted in a mean wear track diameter of 20 mm.

The sliding contact test apparatus was immersed in deoxygenated deionised water with the addition of 8.5 mg LiOH per litre which results in a solution of pH $\sim$ 10.5 at room temperature when prepared. In accord with the modified chemistry regime adopted by many PWRs [17], the concentration of boron in the primary water varies throughout PWR plant operation therefore, boric acid was omitted in this work in order to establish baseline measurements. Band heaters surrounding the autoclave permitted elevated temperature testing (250 ^{o}C) and a thermowell positioned inside the autoclave enabled the measurement of the test temperature. The autoclave was pressurised autogenously and no external pressurisation was employed. Therefore, the test pressure varies with respect to test temperature; a pressure of $\sim$ 50 bar was generated during testing at 250 ^{o}C, whereas at 20 ^{o}C the autoclave pressure was 1 bar. A constant rotational speed of 200 rpm was applied to the disc which results in a sliding speed of 0.21 m s^{-1} at the centre of the wear track. Wear testing was performed for a 5 h duration resulting in a total mean sliding distance of $\sim$ 3770 m. Three tests were performed at 20 ^{o}C and six tests at 250 ^{o}C. Following wear testing, pin and disc samples were ultrasonically cleaned in deionised water before being weighed. This removed any loose debris and third bodies which may have been retained at sliding interfaces of samples. The extent of wear was subsequently quantified by the mass loss of detached material from the pin and disc samples using a balance with a 0.1 mg precision. The volume loss was then evaluated from the mass loss results using a density for Stellite 6 derived by gas displacement pycnometry. The mass and

volume loss measurements therefore encompass two factors, namely (i) the mass and volume loss due to the ejection of material from the contacting surfaces during sliding (wear loss), and (ii) any loose third bodies which have not been ejected during sliding but removed during sample preparation.

In order to determine the mass change as a result of bulk corrosion only (outside the sliding contact zone), a disc was immersed in lithiated water at 250 ^{o}C for 5 h in the same wear apparatus without the application of any mechanical stimuli. This measurement showed that the mass change due to corrosion was < 0.2 mg, thus illustrating that corrosion outside the wear track (non-mechanically affected area) is negligible over the time frame of the sliding contact experiments compared to the tribocorrosion damage. It is, however, recognised that the electrochemical potential may evolve during sliding which may influence corrosion rate.

2.3. Microstructural characterisation

Bulk metallurgical and cross-sectional wear samples were initially machined via electrical discharge machining (EDM) or using a cubic boron nitride cut-off wheel. These samples were subsequently ground, diamond polished to a 1 μm finish, and then given a final polish using 0.06 μm colloidal silica prior to analysis by X-ray diffraction (XRD (Appendix A)) and microstructural analysis in a scanning electron microscope (SEM). Backscattered electron (BSE) and secondary electron (SE) SEM imaging of polished bulk, cross-sections and worn surface morphologies was performed on a tungsten filament FEI Quanta 600 operating at 20 kV. EBSD data were acquired using a Jeol 7100F field emission gun SEM (FEG-SEM) operating at 15 kV equipped with a Oxford Instruments Nordlys Nano EBSD detector.

The X-ray difractograms used for phase identification and Rietveld analysis were recorded using a Bragg-Brentano configured Bruker D8 employing Cu K-α radiation and a LYNXEYE XE-T position sensitive (1D) energy discriminating detector. This machine is equipped with a variable anti-scatter screen, variable divergent slits, and a variable detector window. A working voltage and current of 40 kV and 40 mA respectively were employed. Rietveld refinements [18] were performed using Topas V6 and the fundamental parameters approach to

X-ray line profile fitting [19,20] was employed. Following autoclave wear testing, diffractograms were obtained from exclusively within the tribologically affected material of disc samples. These samples were prepared via electrical discharge machining (EDM) followed by the removal of the re-cast layer surrounding the worn surface in accordance with the metallurgical sample preparation method outlined above.

Electron transparent ($\sim$ 150 nm thick) transmission electron microscope (TEM) lamellae were prepared from regions near the surface of the wear tracks of disc samples using an FEI Scios DualBeam. A standard focused ion beam (FIB) lift-out method was employed. TEM lamellae aligned parallel to the sliding (shear) direction and perpendicular to the worn surface were taken from the centre of wear tracks. Electron beam (EB) platinum deposition was initially used to deposit platinum directly onto the worn surface in order to minimise the subsurface damage caused by subsequent FIB platinum deposition and FIB machining operations. Conventional TEM, scanning transmission electron microscopy (STEM) and elemental mapping via energy dispersive spectroscopy (EDS) was undertaken using a FEG source, FEI Talos F200X TEM operating at 200 kV.

3. RESULTS

3.1. AS-RECEIVED HIPED STELLITE 6: PHASES AND MICROSTRUCTURES

Stellite 6 is principally composed of an (fcc) γ-Co solid solution (Fm3m space group) with a smaller fraction of an orthorhombic M_7C_3 carbide phase (Pmcm space group) and a very small amount of an (hcp) ϵ-Co solid solution (P63/mmc space group) (see diffractogram in Appendix A). The phase fractions of as-received Stellite 6 were approximated via Rietveld analysis and are reported in Table 2.

Table 2: Phase fractions and crystallographic data of phases identified within HIPed Stellite 6 as determined via Rietveld analysis.

	γ-Co	**M_7C_3**	**ϵ-Co**
wt %	88.8	10.8	0.4
vol %	86.3	13.3	0.4
Space Group	Fm-3m	Pmcn	P63/mmc
Lattice Parameters (nm)	a = 0.3559	a = 0.7025	a = 0.2495
	b = 0.3559	b = 1.2151	b = 0.2495
	c = 0.3559	c = 0.4503	c = 0.4503

The SEM-BSE micrographs of Stellite 6 shown in Fig. 1 (a) and (b) reveal dark-contrast equiaxed chromium-rich precipitates (M_7C_3), ranging in size between $\sim$ 1 and 4 μm, in a Co-rich matrix where grain and annealing twin boundaries are clearly visible due to channelling contrast. At higher magnification (Fig. 1 (b)), there is evidence of deformation banding in the matrix around the M_7C_3 precipitates; this presumably results from the mismatch in thermal expansion between the two main phases during the cooling period of the HIP cycle.

Fig. 1 (c) and (d) show an EBSD-derived phase map of HIPed Stellite 6 and accompanying inverse pole figure (IPF) respectively. As previously identified via XRD and SEM-BSE, HIPed Stellite 6 (Fig. 1 (c)) is principally composed of a Co-rich solid solution matrix (blue) which surrounds an M_7C_3 type carbide

phase (yellow). EBSD (Fig. 1 (c)) has identified several small grains which are crystallographically consistent with the ϵ-Co phase previously identified by XRD. The inverse pole figure (Fig. 1 (d)) clearly illustrates the high angle annealing twins and grain boundaries within the Co-based solid solution matrix.

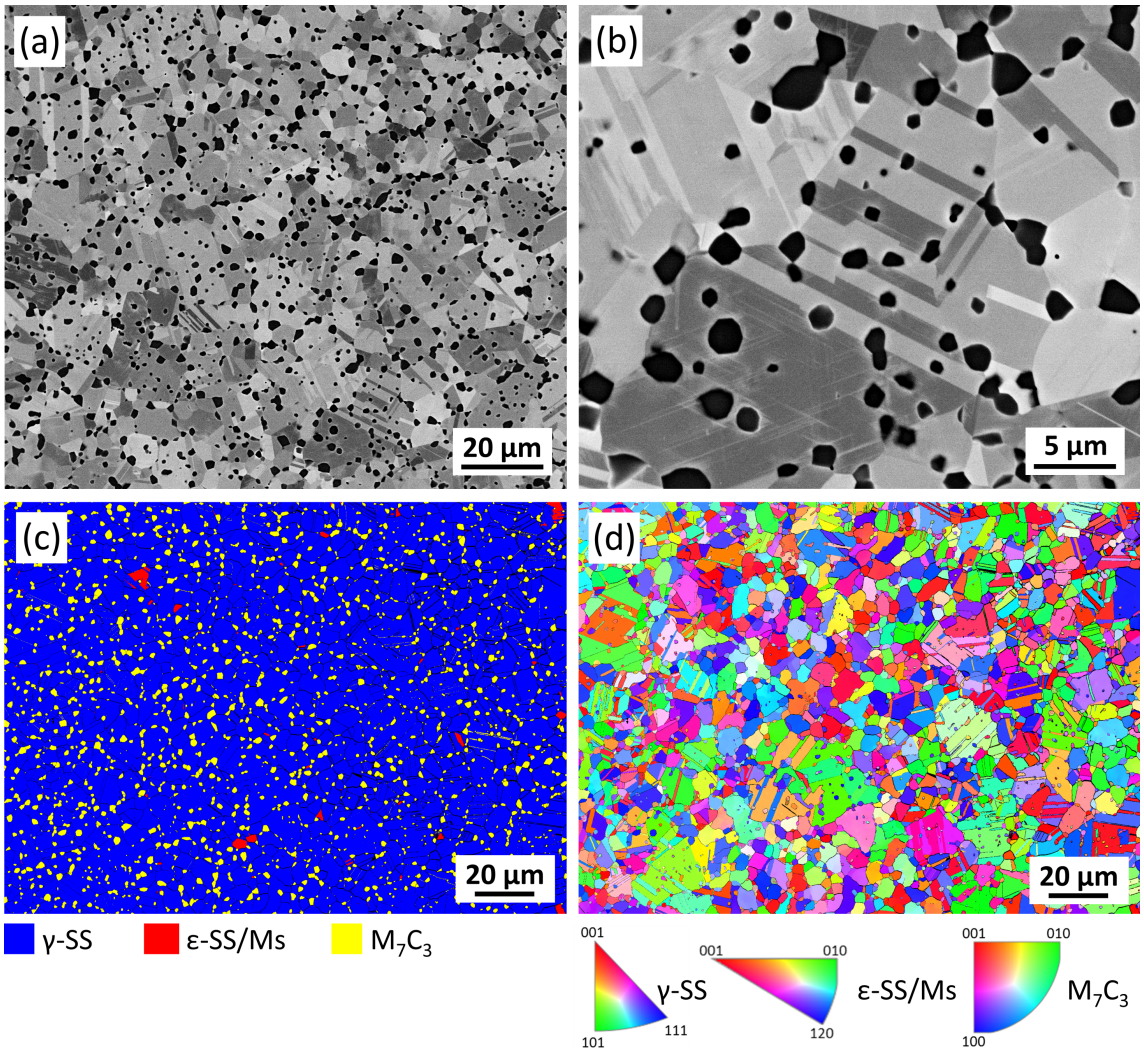

Figure 1: BSE-SEM channelling contrast micrographs (a and b) and both EBSD-derived phase (c) and IPFZ (d) maps of HIPed Stellite 6. (a) and (b) show M_7C_3 carbides (darkest contrast) and cobalt-based matrix grains with annealing twins. (c) shows M_7C_3 carbides (yellow) surrounded by a fcc Co-based solid solution matrix (blue (γ-SS)) and a small fraction of a hcp Co-based solid solution (grains) and ϵ-martensite laths (red (ϵ-SS/Ms)). (d) depicts the same region shown in (c) and shows matrix grains with high angle annealing twins.

3.2. AUTOCLAVE SLIDING CONTACT TEST RESULTS - MASS AND VOLUME LOSS

The combined pin and disc mass and volume losses for Stellite 6 after 5 h, 4 kg dead load sliding contact tests at 20 ^{o}C and 250 ^{o}C within an autoclave environment are shown in Fig. 2. The volume loss measurements were derived from mass loss values and converted to volume loss using a measured Stellite 6 density of 8370 $\pm$1 kg/m^3 (as evaluated by gas displacement pycnometry). The combined pin and disc volume and mass loss increased by a factor of between $\sim$ 16.5 - 38.7 when the test temperature was raised from 20 to 250 ^{o}C.

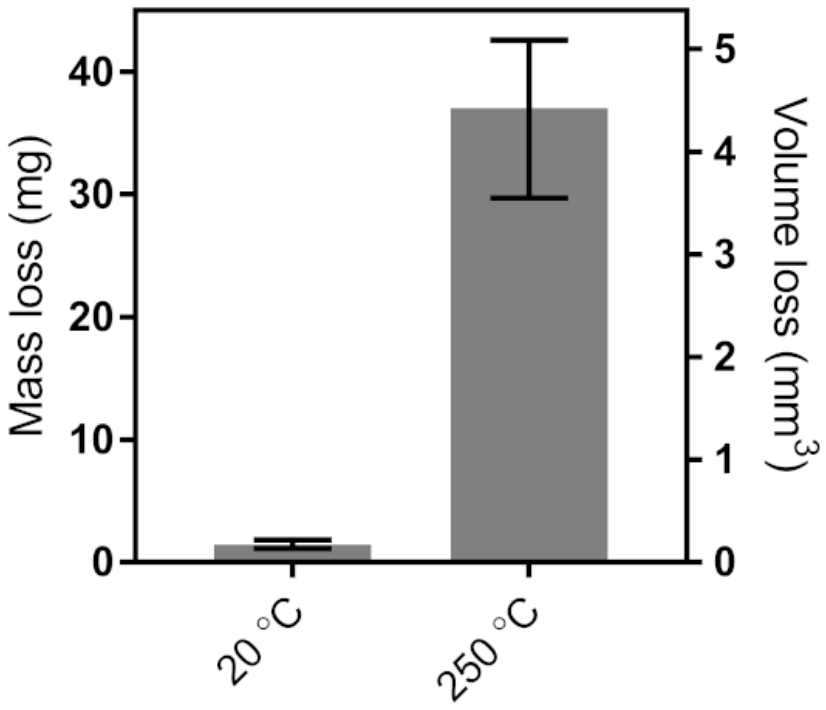

Figure 2: Graph showing the effect of autoclave test temperature on the mass and volume loss following 5 h sliding contact testing with a 4 kg dead load. The bars represent mean values and the error bars represent the minimum and maximum values of combined pin and disc wear. Three tests were conducted at 20 ^{o}C and six at 250 ^{o}C

3.3. MICROSTRUCTURAL CHARACTERISATION OF THE CONTACTING SURFACES - SURFACE TOPOGRAPHY

Fig. 3 shows representative low magnification optical stereoscope micrographs of Stellite 6 disc (Fig. 3 (a) and (b)) and pin (Fig. 3 (c) and (d)) samples after sliding contact tests at 20 (Fig. 3 (a) and (c)) and 250 ^{o}C (Fig. 3 (b) and (d)). These micrographs confirm the trends observed in the volume and mass loss measurements presented in Fig. 2 and clearly show that the amount of material removed increases with increasing temperature. Fig. 3 shows that the wear track becomes significantly wider and the contact area is much greater at the higher temperature. The disc wear tracks measure $\sim$ 1.7 mm and $\sim$ 6.3 mm in width following testing at 20 ^{o}C and 250 ^{o}C respectfully. At both test temperatures, the tribologically/chemically affected surfaces of both the pin and disc are analogous to one another therefore it is suggested that the general mechanisms of degradation are similar as well. This is consistent with previous findings in the literature and only results obtained from disc samples will be reported hereafter [21].

Plan view BSE-SEM micrographs taken from central regions within the wear tracks of Stellite 6 discs are shown in Fig. 4 (sliding direction horizontal). The worn surfaces appear remarkably similar despite the material loss being between $\sim$ 16.5 - 38.7 times greater at the higher temperature. At both temperatures, the surface features can principally be characterised by scoring and scratching and there is no evidence of any surface features indicative of macroscale plasticity dominated wear. There is little evidence for decohesion of the carbide from the matrix although occasionally carbide pull-out is observed, as indicated by the red arrows in Fig. 4 (a) and (b). Additionally, the fracture of carbides is also occasionally observed at the contacting surface. Depressions and discontinuities in the worn surface appear to accumulate dark contrast material which is possibly oxide. There is no evidence for preferential wear/corrosive attack on the carbide, the matrix, or at the carbide-matrix interface within the resolution of the SEM. Additionally, the matrix and carbide phases appear to recede (wear/corrode) evenly in conjunction with one another. Comparison of Fig. 4 (c) and (d) show

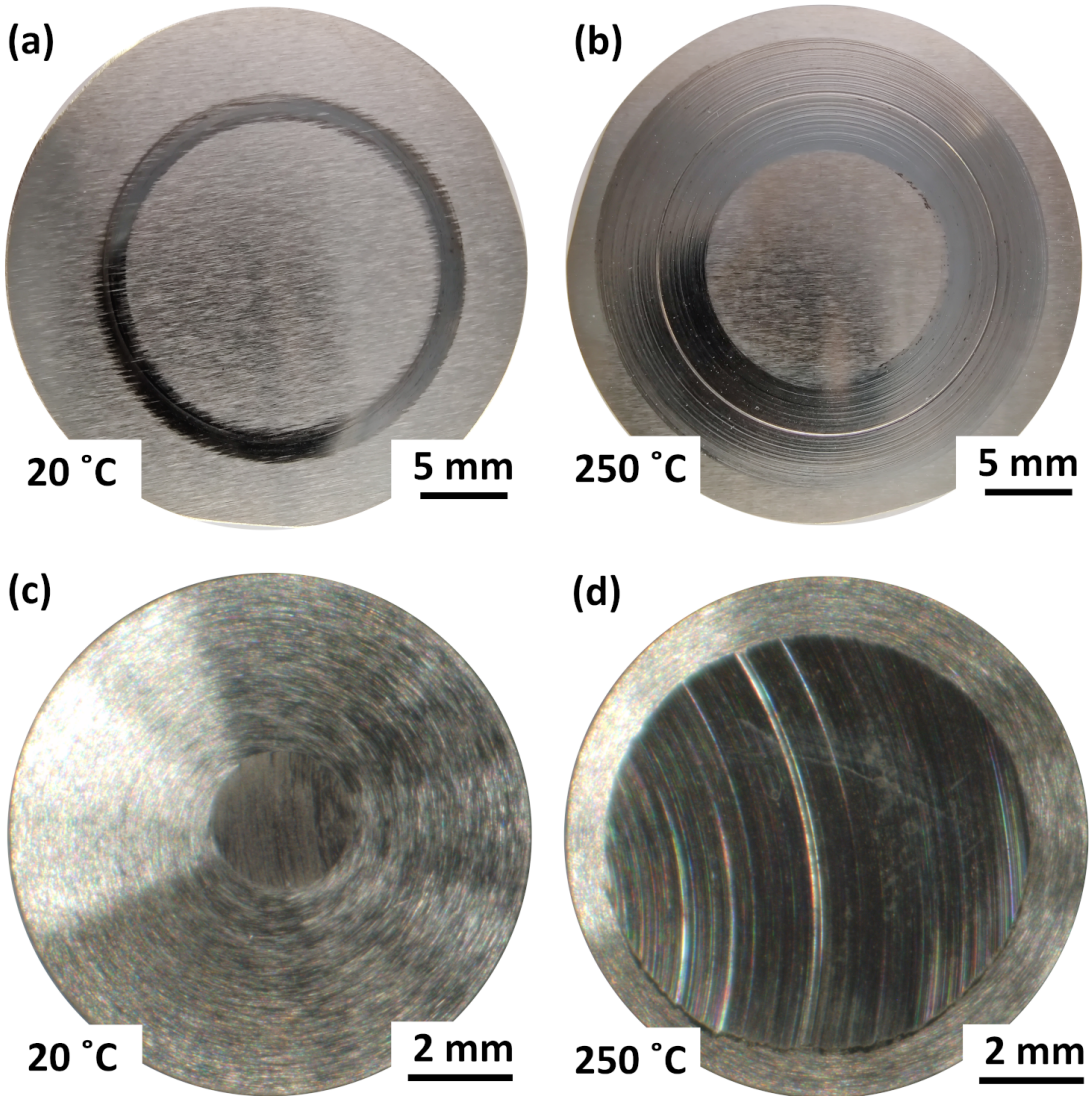

Figure 3: Stereoscope optical micrographs of Stellite 6 disc ((a) and (b)) and pin ((c) and (d)) tribologically/chemically affected surfaces following sliding contact autoclave tests at 20 ((a) and (c)) and 250 ^{o}C ((b) and (d)).

only subtle differences in features on the contacting surfaces. Firstly, the scoring and scratching along the sliding direction is more frequent and deeper in the sample tested at 250 ^{o}C. Secondly, there is also a more noticeable mottled contrast on the matrix surface at 250 ^{o}C than at 20 ^{o}C. This mottled contrast is possibly related to oxidation and/or mixing at the contacting surface during sliding. Some contrast variation is also observed over the M_7C_3 phase. In summary, the worn surface features strongly suggest that the mechanisms of material removal are essentially the same at the different temperatures, which is entirely consistent with previous studies [21,22].

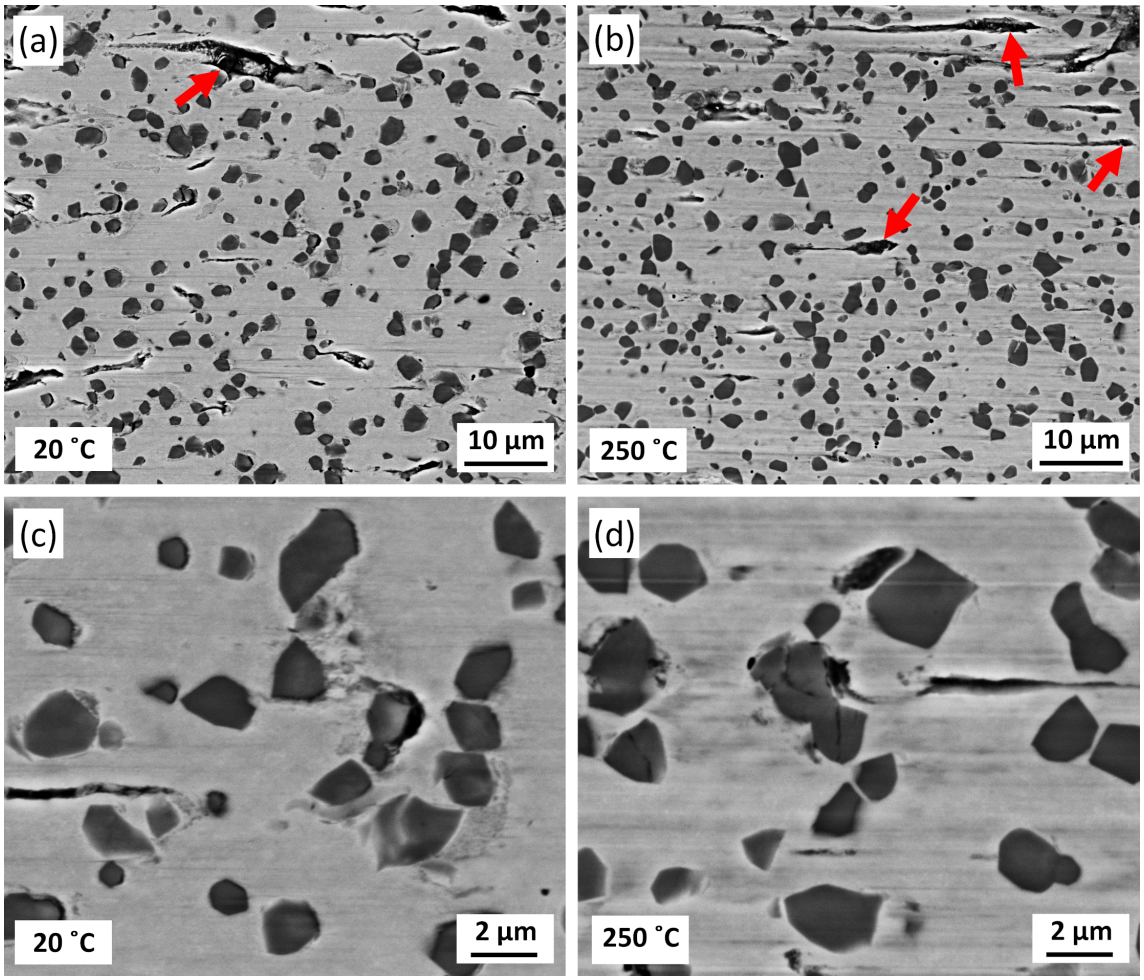

Figure 4: Plan view BSE-SEM micrographs showing the microstructure of the tribologically/chemically affected surface of Stellite 6 disc samples after sliding contact tests in an autoclave environment at 20 ^{o}C (a and c) and 250 ^{o}C (b and d) for 5 hours. Sliding direction was horizontal on the image. Carbide pull-outs are indicated by red arrows.

3.4. X-RAY DIFFRACTION FROM THE WORN SURFACE

The X-ray diffractograms shown in Fig. 5 were obtained from the as-received HIPed material and exclusively from within the wear tracks following testing at 25 and 250 ^{o}C. As expected, all the phases observed in the as-received HIPed material are still present following autoclave testing at both temperatures. Large reflections that are consistent with hcp ϵ-Co are also observed in the XRD patterns from within the wear track and are due to strain induced martensitic (SIM) transformation. A significant fraction of ϵ-Co is generated in response to autoclave sliding at both testing temperatures, however from the inspection of peak height ratios, it

is evident that the extent of this transformation is less at 250 ^{o}C than at 20 ^{o}C. At both test temperatures, the ϵ-Co phase exhibits a preferred orientation due to preferred alignment of primary slip systems parallel to the direction of shear. Autoclave testing has clearly had a profound effect on the peak shapes, peak position, maximum peak intensities and peak asymmetry of the matrix phase reflections relative to the polished surface of Stellite 6. This change in peak shape is a result of crystallographic faulting and crystallite size and strain broadening effects induced by autoclave sliding contact.

The extent of the $\gamma \rightarrow \epsilon$ transformation at the different test temperatures was quantitatively compared using the Rietveld method to analyse the XRD patterns. Even though the X-ray intensity contributing to the diffracted signal decreases exponentially with increasing depth into the sample [23], the average X-ray penetration depth contributing 99 % of the diffracted intensity was on average $\sim$ 5 μm over the range of 2θ values (35-120 ^{o}) used in the Rietveld refinements [23]. However, the samples are expected to have similar X-ray interaction volumes regardless of the test temperature and therefore a comparative quantitative assessment for the volume percent of fcc γ matrix transformed to ϵ-martensite can be made. At 20 ^{o}C and 250 ^{o}C, the volume percent of matrix transformed to ϵ-martensite from within the interaction volume contributing to the diffracted signal was $\sim$ 95 % and $\sim$ 88 % respectively.

3.5. Sub-surface microstructural characterisation of Stellite 6

Cross-sectional BSE-SEM micrographs taken from within the wear track parallel to the sliding direction for Stellite 6 tested at 20 ^{o}C and 250 ^{o}C are shown in Fig. 6. In all cases, the (worn) contacting surfaces appear continuous and flat with no evidence for any preferential wear/corrosive attack of the carbide, the matrix, or the carbide-matrix interface. There is also no evidence of any extensive plastically transferred material on the sliding surface when observed via SEM. At both test temperatures, the severe plastic deformation (due to the sliding contact) within the

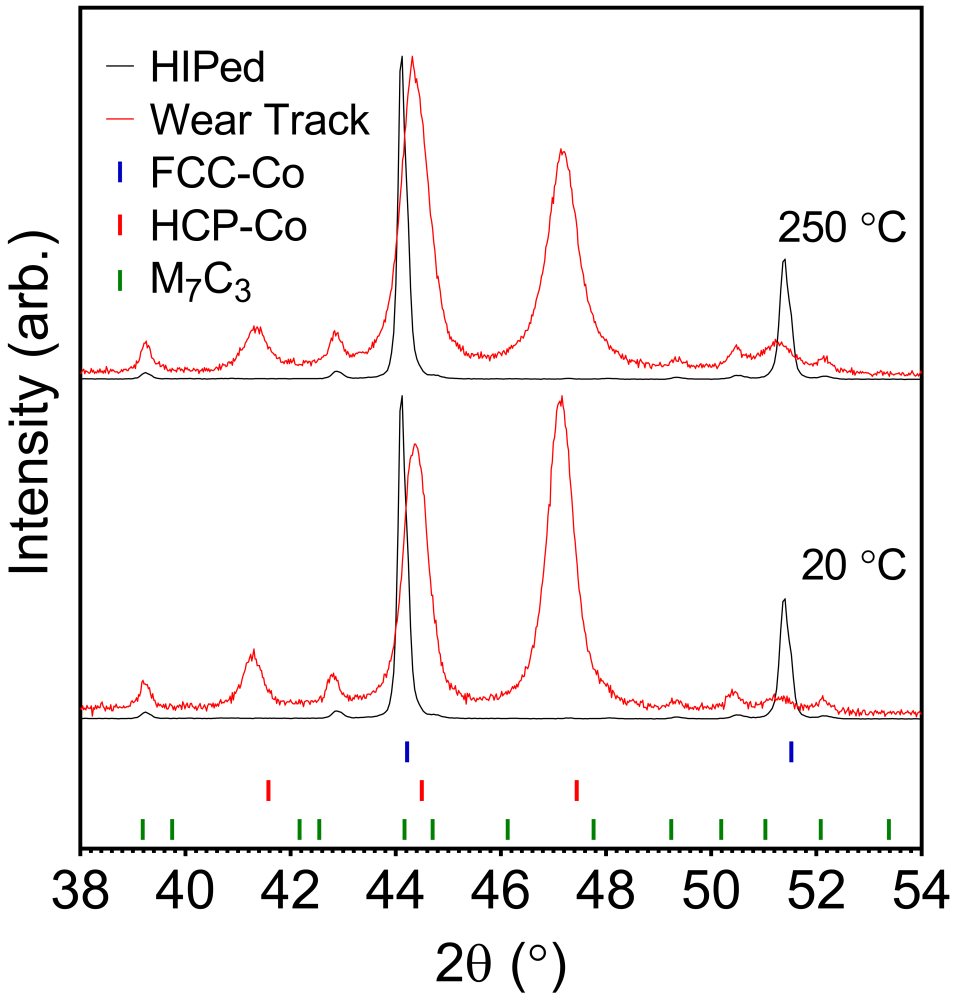

Figure 5: XRD patterns from the polished surface of the as-received Stellite 6 (black) and from within the wear track of disc samples (following testing at 20 ^{o}C and 250 ^{o}C)(red). Patterns normalised to the reflection of maximum intensity.

subsurface is observed to be accommodated by the generation of planar defects in the matrix which are visible due to channelling contrast. Within approximately the top 5 and 8 μm of the subsurface of the samples tested at 20 (Fig. 6 (a) and (c)) and 250 ^{o}C (Fig. 6 (b) and (d)) respectively, the extent of plastic deformation is sufficiently severe to make grain/cell boundaries almost indistinct. At both test temperatures, a deformation gradient is clearly generated from the loaded sliding contact; this is evident from the decrease in deformation features (which act to spatially homogenise matrix contrast variation) with increasing depth below the surface. The deformation structures appear largely the same irrespective of test

temperature (Fig. 6 (c) and (d)). However, the density of planar defect traces such as twins and martensite laths at any given depth from the contacting surface is larger following testing at 250 ^{o}C. This suggests that at 250 ^{o}C the subsurface is subjected to somewhat higher levels of strain during sliding and that the plastically deformed zone is deeper penetrating.

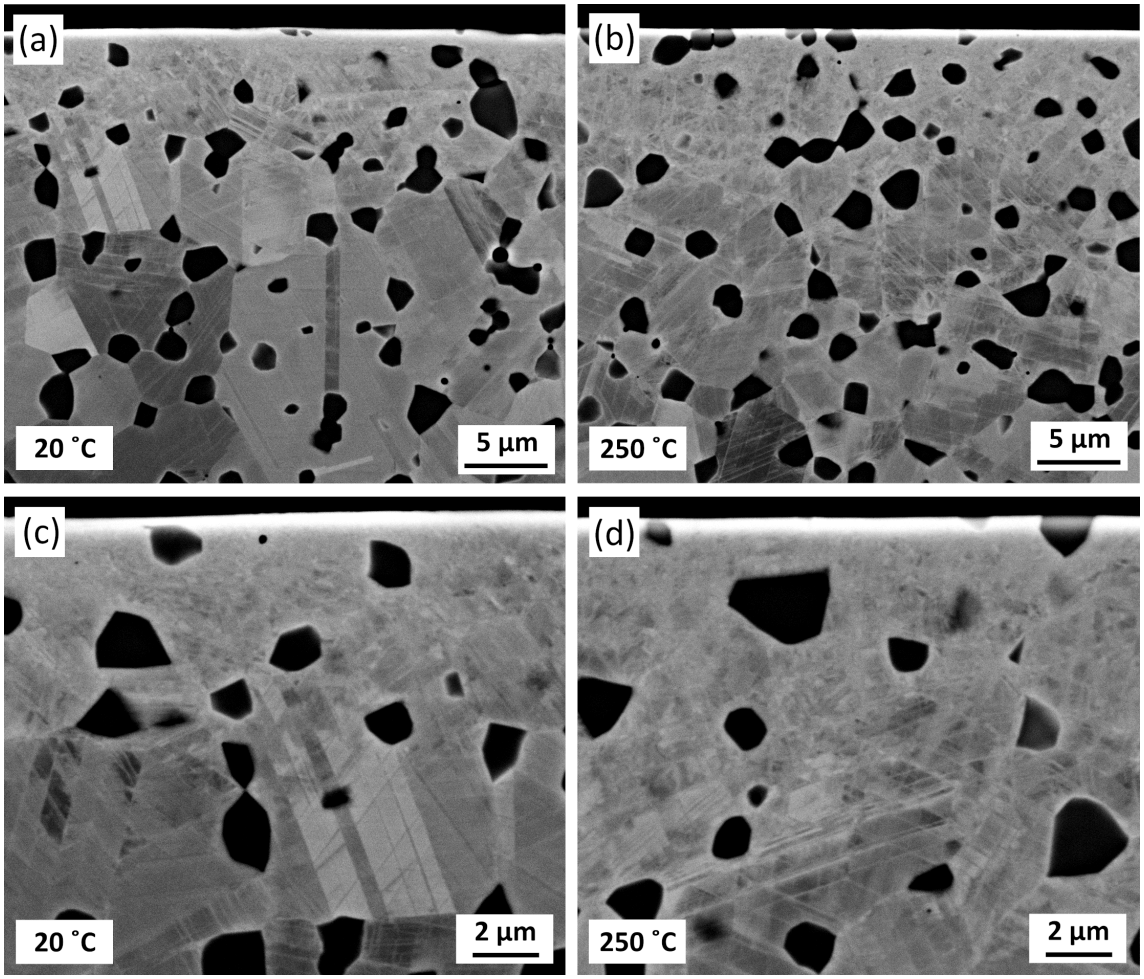

Figure 6: Cross-sectional BSE-SEM channelling contrast micrographs of Stellite 6 taken from within the wear track of disc samples (parallel to the sliding direction) after testing at 20 ^{o}C (a, c) and 250 ^{o}C (b, d). M_7C_3 (dark contract) carbides are distributed in Co-rich matrix with traces of planar deformation structures.

Fig. 7 shows EBSD derived phase maps (Fig. 7 (a) and (b)), band contrast maps (Fig. 7 (c) and (d)) and inverse pole figures (Fig. 7 (e) and (f)) taken perpendicular to the sliding direction of Stellite 6 samples following autoclave sliding wear testing at 20 (Fig. 7 (a), (c) and (e)) and 250 ^{o}C (Fig. 7 (b), (d) and (f)). EBSD reveals three crystallographically distinguishable structures which are identical

to those identified in XRD (Fig. 5) namely, (i) fcc γ-Co (blue), (ii) hcp ϵ-Co (red) and (iii) M_7C_3 carbide (yellow). Fig. 7 demonstrates that a large fraction of the resolvable planar defects are laths of ϵ-Co which are presumably generated via the $\gamma \rightarrow \epsilon$ strain induced transformation previously identified by XRD (Fig. 5). Fig. 7 confirms the observations made via conventional SEM (Fig. 6) and shows a clear deformation gradient whereby the extent of deformation-induced microstructural refinement of the matrix increases towards the sliding surface. Additionally, the band contrast micrographs (Fig. 7 (d) and (d)) show a relative increase in the degree of subsurface deformation following testing at 250 ^{o}C. Despite the increase in subsurface deformation observed following testing at 250 ^{o}C (Fig. 6 and Fig. 7 (c) and (d)), the phase maps (Fig. 7 (a) and (b)) show that the extent of $\gamma \rightarrow \epsilon$ strain induced transformation is greater after sliding at 20 ^{o}C relative to 250 ^{o}C; this was also deduced from XRD patterns (Fig. 5). Irrespective of test temperature, the phase maps (Fig. 7 (a) and (b)) suggest that the matrix at the contacting surfaces has completely transformed to ϵ-martensite. However, near the surface there is a large fraction of black pixels that correspond to regions that could not be indexed by EBSD. Hence to resolve these features TEM was undertaken as described in next section.

3.6. TEM CHARACTERISATION

Bright field (BF)-STEM micrographs of the subsurface microstructure obtained from cross-sectional FIB samples of Stellite 6 taken parallel to the direction of sliding are shown in Fig. 8 and allow sub-micron features to be revealed. After testing, the principal near surface microstructural features remain similar irrespective of test temperature with M_7C_3 particles embedded in a highly deformed Co-based matrix (Fig. 8 (a) and (b)). However, inspection of the effective grain size shows that at any given depth from the contacting surface the deformation induced matrix microstructural refinement is more extensive following testing at 250 ^{o}C than at 20 ^{o}C. This implies that higher subsurface strains are induced during sliding at 250 ^{o}C (Fig. 8). By way of rough approximation, at a distance of ≥ 1 μm and ≥ 2 μm following testing at 20 ^{o}C and 250 ^{o}C respectively, the

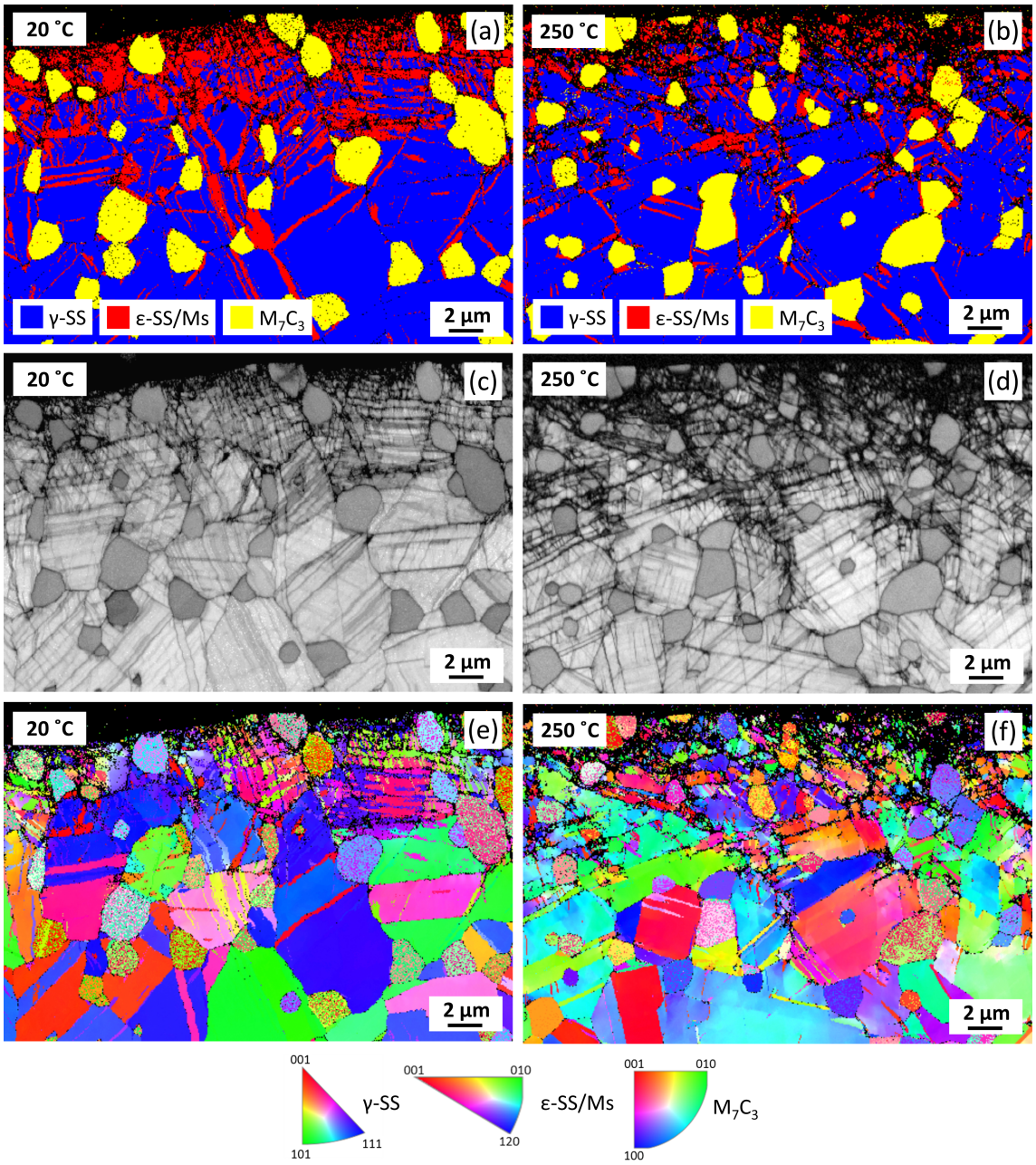

Figure 7: EBSD derived phase maps ((a) and (b)), band contrast maps ((c) and (d)) and inverse pole figures ((e) and (f)) taken perpendicular to the sliding direction of HIPed Stellite 6 disc samples following autoclave sliding wear testing at 20 ((a), (c) and (e)) and 250 ^{o}C ((b), (d) and (f)). Regions which could not be indexed are shown in black.

matrix nanostructure is principally composed of rhombic, trigonal and quadrilateral domains which are generated via extensive deformation banding and SIM transformation (Fig. 8(a) and (b)). This matrix nanostructure is also heavily flawed with stacking faults as indicated by the fine parallel striations contained within

individual blocks (Fig. 8 (a) and (b)). At depths ≤ 1 μm and ≤ 2 μm beneath the contacting surface following testing at 20 (Fig. 8 (a) and (c)) and 250 ^{o}C (Fig. 8 (b) and (d)) respectively, there appears to be a shift in the principal deformation mode which appears to result in the generation of fine equiaxed nanocrystals which exhibit a high degree of internal and boundary disorder.

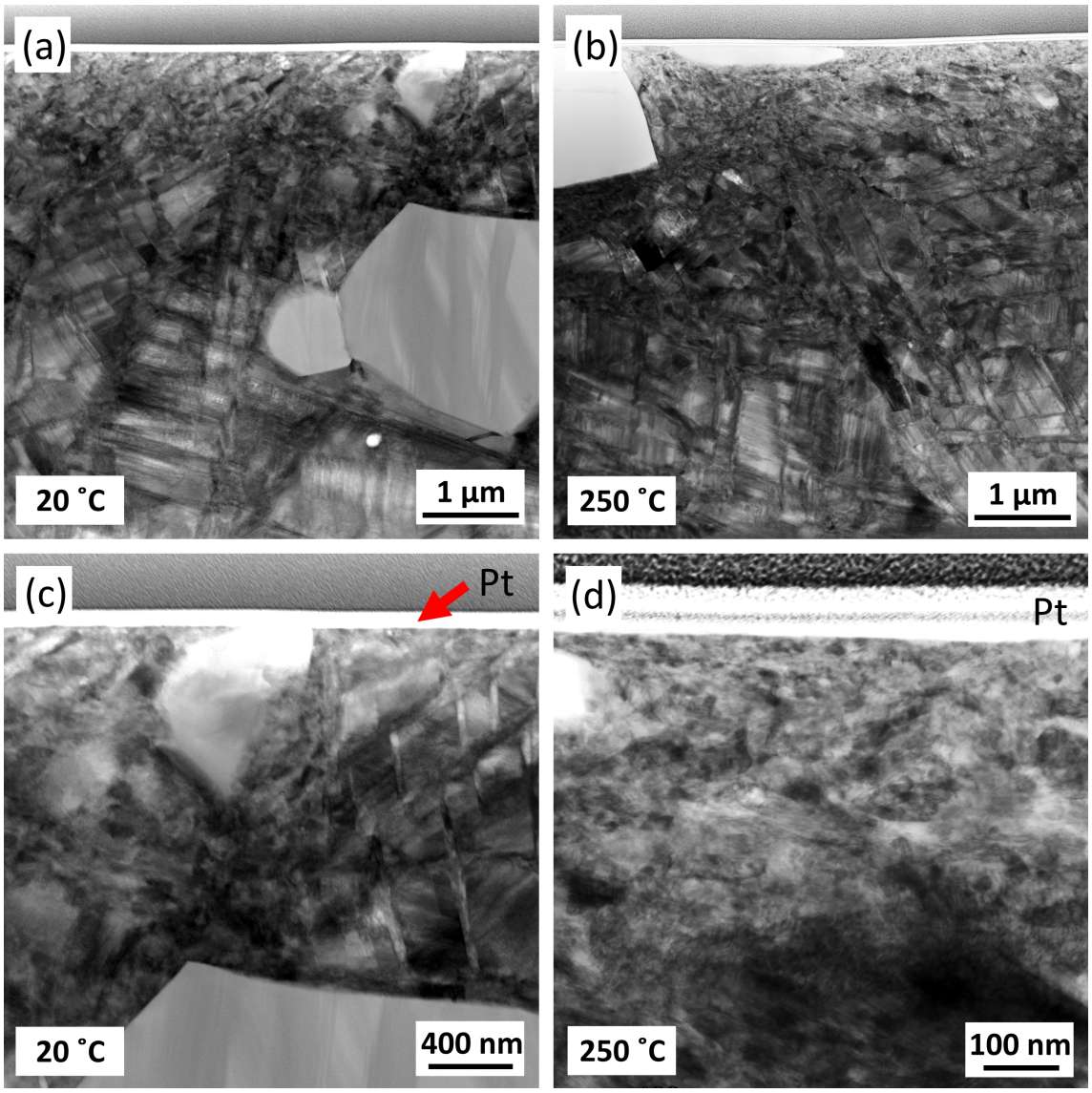

Figure 8: Representative BF-STEM micrographs of Stellite 6 disc samples taken from within the wear track (parallel to the sliding direction) after testing at 20 ^{o}C (a, c) and 250 ^{o}C (b, d). Angular, micron sized M_7C_3 particles are visible within the highly faulted cobalt-rich matrix

The BF-TEM images (Fig. 9 (a) and (c)) reveal the microstructural detail of the most heavily deformed nanocrystalline region below the contacting surface following testing at 20 ^{o}C and 250 ^{o}C respectively. The selected area diffraction

patterns (SADP) of these regions presented in Fig. 9 (b) and (d) (following testing at 20 ^{o}C and 250 ^{o}C respectively) confirm that these nanostructures are ϵ-martensite (hcp). This supports the hypothesis that the matrix completely undergoes the SIM ($\gamma \rightarrow \epsilon$) transformation to ϵ-martensite at both test temperatures. The diffraction rings are clearly more continuous following testing at 250 ^{o}C (Fig. 9 (d)), thus showing that the effective grain size within the top $\sim$ 300 nm is more heavily refined after testing at the higher temperature.

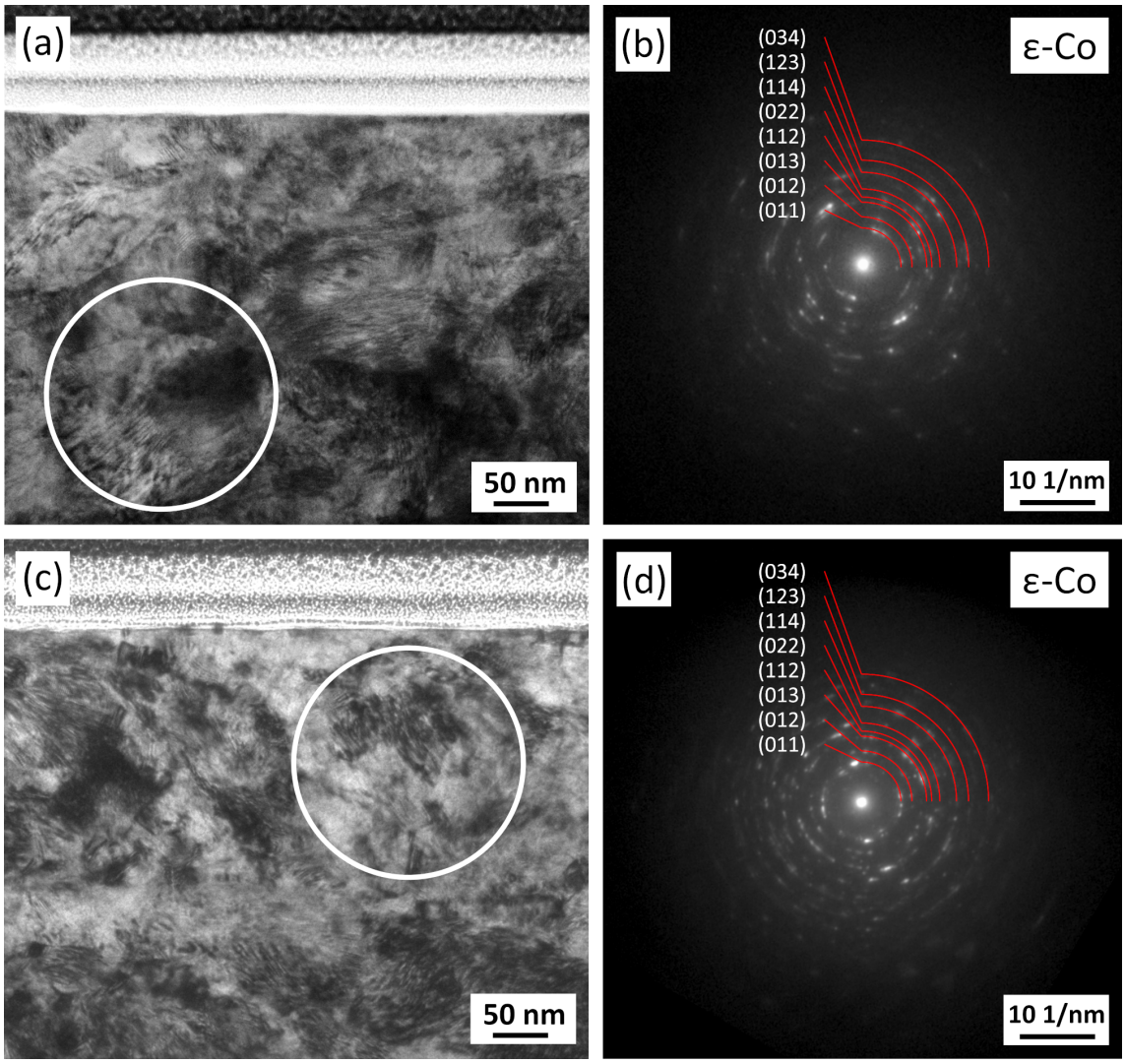

Figure 9: Representative BF-TEM micrographs ((a) and (c)) and SADPs ((c) and (d)) from samples taken parallel to the direction of shear, showing the deformation structures directly beneath the contacting surface of Stellite 6 disc samples after exposure to sliding contact at 20 ^{o}C ((a) and (b)) and 250 ^{o}C ((c) and (d)). The SADPs, (b) and (d), index to hcp ϵ-Co and have been recorded from the regions marked with circles in (a) and (c) respectively.

The BF-STEM micrograph and accompanying EDX maps (Fig. 10) show a $\lesssim$ 10 nm thick oxygen-rich layer on the contacting surface following testing at 250 ^{o}C which is most probably a passive oxide layer. The passive nature of Stellite 6 in a high temperature ($\sim$ 300 ^{o}C) lithiated water environment has been reported previously [24–26].

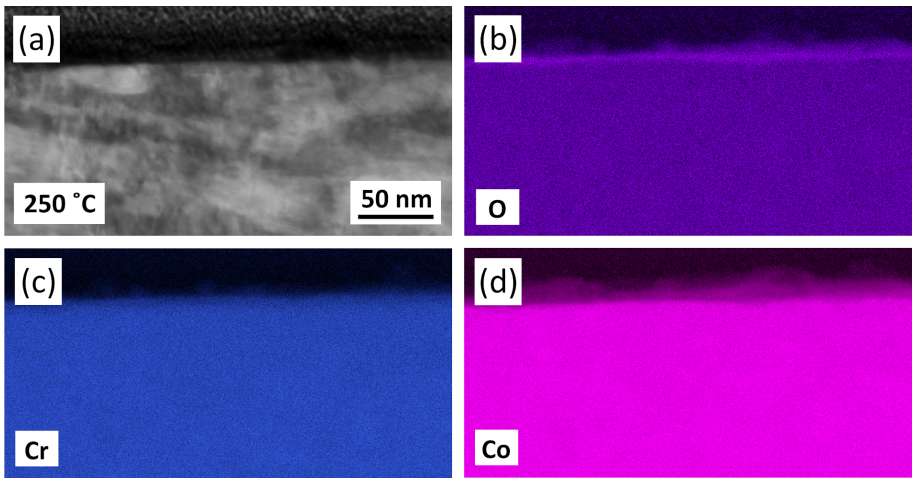

Figure 10: (a) BF-STEM micrograph of a Stellite 6 disc sample taken parallel to the direction of shear following exposure to sliding contact at 250 ^{o}C. (b), (c) and (d) show EDX maps of the same region depicted in (a) and correspond to maps for O, Cr and Co respectively.

The HAAD-STEM micrograph (Fig. 11 (a)) and accompanying Co EDX map Fig. 11 (b) show the microstructural detail of the matrix surrounding a high aspect ratio M_7C_3 carbide previously shown at lower magnification in Fig. 8 (b) following testing at 250 ^{o}C. This particular M_7C_3 particle has clearly worn extensively during sliding as such high aspect ratio carbides are not observed in the as received material (Fig. 1). Fig. 11 (c) and (d) are higher magnification BF-TEM micrographs of this same carbide which show a thin nanolayer $\sim$ 20 nm thick at the contacting surface (red arrows) which spans the entire length of the carbide (Fig. 11 (a)). The Co content within this nanolayer decreases across the length of the carbide. Additionally, the microstructural features within this nanolayer become increasingly finer across the length of the carbide (Fig. 11 (c)) and eventually become indistinguishable with no contrast variation (Fig. 11 (c) and (d)). Fig. 11 (d) shows what appears to be some discontinuity between the carbide and nanolayer in the form of a dark contrast hairline linear indication.

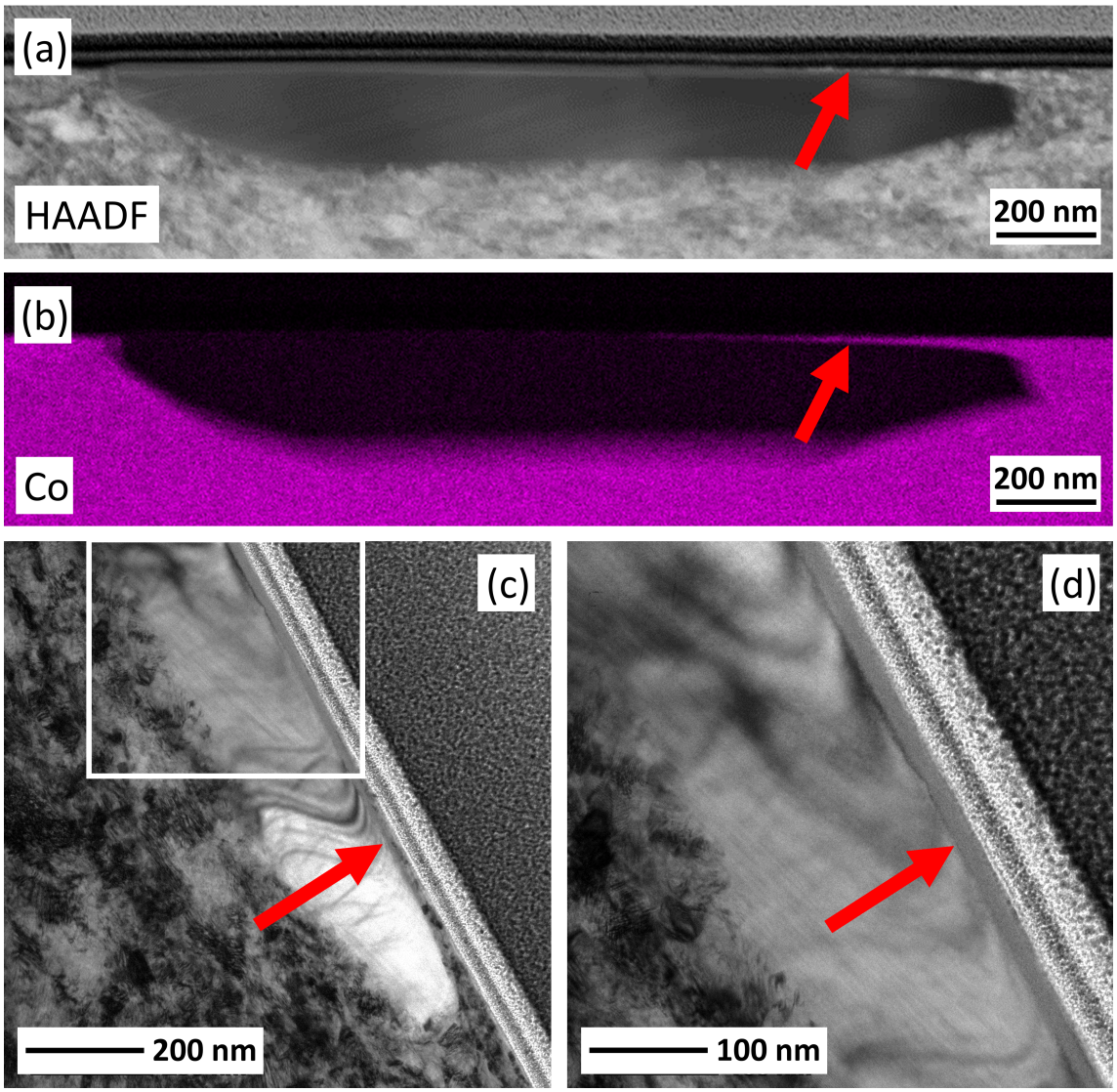

Figure 11: Micrographs taken parallel to the direction of sliding from a Stellite 6 disc sample which show the formation of a mechanically mixed nanolayer (red arrow) over an M_7C_3 carbide at the contacting surface following testing at 250 ^{o}C. (a) depicts a HAADF-STEM micrograph and (b) shows an accompanying Co map. (c) and (d) show higher magnification BF-TEM micrographs of this same carbide.

Fig. 12 depicts both BF-STEM (Fig. 12 (a)) and HAADF-STEM (Fig. 12 (b)) micrographs taken parallel to the sliding direction showing a thin $\sim$ 100 nm thick fractured M_7C_3 carbide situated at the contacting surface of Stellite 6 following testing at 20 ^{o}C. This high aspect ratio carbide morphology must be generated during sliding wear and is similar to the carbide also shown in Fig. 11.

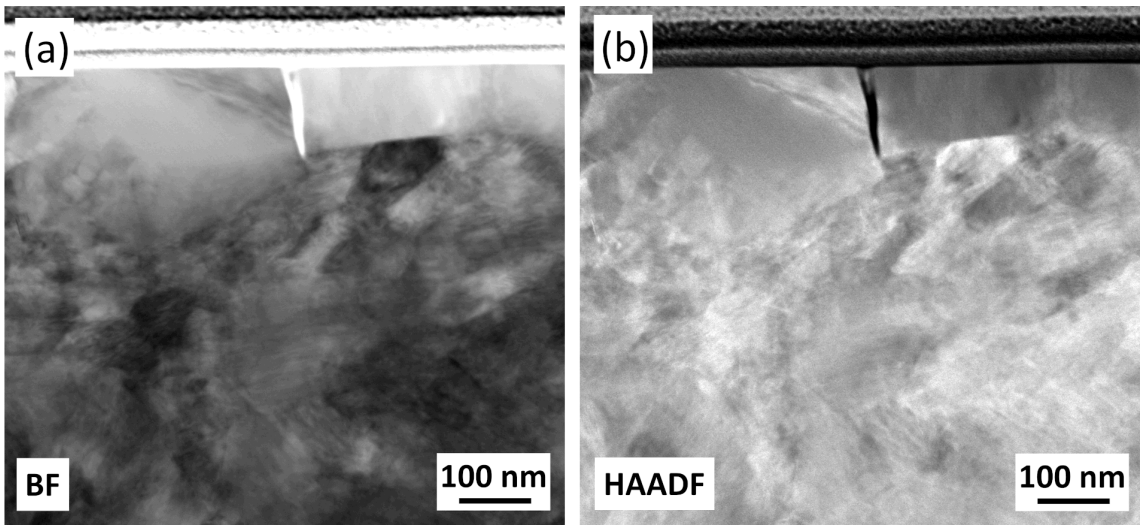

Figure 12: BF-STEM (a) and HAADF-STEM (b) micrographs taken parallel to the sliding direction from a Stellite 6 disc sample showing a $\sim$ 100 nm thick fractured M_7C_3 carbide in the nanocrystalline Co-rich matrix situated at the contacting surface following testing at 20 ^{o}C.

4. Discussion

This study has shown that the combined pin and disc material loss from Stellite 6 during self-mated sliding contact in lithiated water is higher at 250 ^{o}C than at 20 ^{o}C, by a factor of between $\sim$ 16.5 - 38.7 when assessed through volume loss measurements. Stellite 6 remains highly corrosion resistant at both 20 ^{o}C and 250 ^{o}C and Fig. 10 shows a thin oxide film which is consistent with passivating behaviour [24–26]. The most notable macro/microscopic difference between the two different test temperatures is the extent of scratching and scoring within the wear track. Although there are differences in the depth to which subsurface deformation features are observed and the extent of strain induced martensite, the subsurface deformation structures, and the phases present within the tribologically affected material (TAM) appear largely comparable irrespective of test temperature (Figs. 6 to 9). However, the site specific TEM study of the most heavily deformed regions (a few micron from the contacting surface) provides new insights into the sub-surface deformation behaviour and the tribological degradation mechanisms operating during sliding contact in a simulated PWR primary circuit environment. Despite the fact that TEM micrographs of the contacting surface do not necessarily encompass the stochastic variability with within the wear track, such studies offer valuable insight into the nanoscale modes of deformation and material removal within the top $\sim$ 2 μm which cannot otherwise be assessed via other lower resolution imaging techniques. The following sections will consider the complex interaction of mechanical deformation and chemical degradation to facilitate better understanding of the mechanisms responsible for the wear (tribocorrosion) behaviour of Stellite 6. Particular attention will be given to analysing the complex sub-surface deformation behaviour of the Co-base matrix under the high strain conditions imposed by the sliding contact.

In light of the results, it is suggested that the main mechanisms of degradation can be described by, (i) tribochemical reactions, and (ii) abrasion. The latter brings about plastic deformation and depassivation by the sub-mechanisms of microploughing and microcutting which further results in the additional sub-

mechanisms of mechanical mixing and tribocorrosion of the first main mechanism. This simplified description of degradation will be discussed in the following sections.

4.1. Matrix deformation and role of the carbide phase during sliding contact

In comparing the tribologically/chemically affected material (TAM) at the two different test temperatures it should be noted that the nominal contact pressures are different due to differences in pin wear (although the local asperity contact pressures will be relatively unaffected [27]). In both cases the strain gradient from the sliding contact induces clearly observable deformation structures up to a depth of at least $\sim$ 30 μm from the sliding interface (Fig. 6 (a) and (b)), which is consistent with that observed in previous related work [21,22].

To simplify the following discussion, it is convenient to sub-divide the continuum of plastically deformed matrix material within the TAM into three layers as schematically illustrated in Fig. 13. The deformation structures discussed in this section are representative of those observed following testing at both 20 ^{o}C and 250 ^{o}C

4.1.1. Layer 1

The undeformed microstructure away from the TAM comprises around 13 vol% of equiaxed M_7C_3 precipitates ($\sim$ 1-4 μm in size) in a Co-based solid solution matrix (fcc, γ-Co) which is made up of equiaxed grains with annealing twins (Table 2 and Fig. 1) and merges into layer 1 at around 30 μm from the surface.

Layer 1 is the region of the TAM furthest from the sliding contact where the original grain and annealing twin boundaries are still distinguishable, and which is subjected to the lowest levels of strain. It occupies depths $\gtrsim$ 5 and 8 μm following testing at 20 ^{o}C and 250 ^{o}C respectively (Figs. 6 and 7) and grain refinement occurs principally via the formation of deformation bands (Figs. 6 and 7). These bands are the primary deformation mode in layer 1 and principally form as a

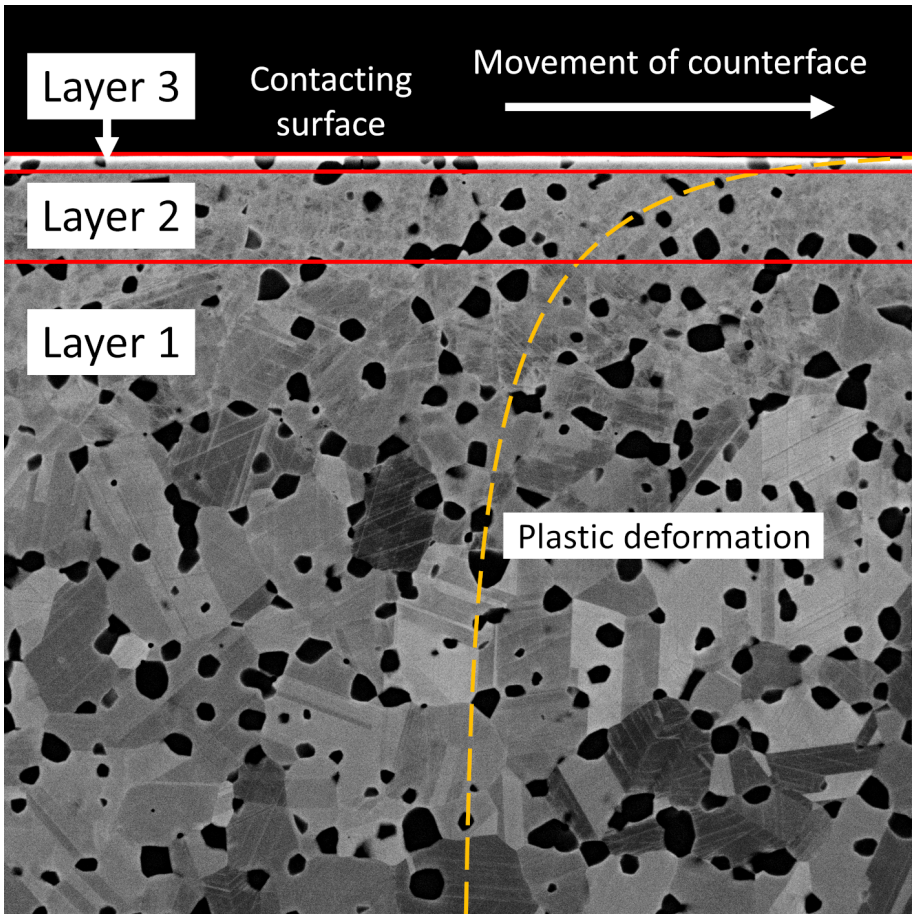

Figure 13: Schematic illustrating the different layers within the TAM used to describe the continuum of plastic deformation within the subsurface. The dashed line is a schematic representation of the extent of plastic flow within the subsurface (not to scale). The further right the line is, the greater the plastic deformation.

result of the strain-induced martensitic transformation (SIMT) γ(fcc)$\rightarrow$ ϵ(hcp) (Fig. 7) which has been extensively observed in Stellite 6 and other related Co-based alloys [21, 22, 28–34]. The SIMT in Stellite 6 occurs via the glide of Shockley partials on every other close packed $\{111\}$ plane and is known to occur up to temperatures of $\sim 700\ ^{o}$C [33, 35–37]. Additionally, ϵ-martensite reportedly forms preferentially at annealing twin boundaries in the early stages of transformation (Fig. 7) [38]. However, some studies suggest that a SIMT may not be the initial mode of deformation in low stacking fault energy (SFE) Co-based fcc alloys [28, 29, 39]. Therefore, it is possible that within the regions subjected to the very lowest strains (i.e. furthest from the interface), the fcc γ phase could accommodate initial plastic deformation via dislocation glide on the $\{111\}_{\gamma}$ planes, forming

intersecting planar arrays of dislocations [29]. As the strain is increased (i.e. closer to the interface), it is suggested that the deformation mode changes first from dislocation slip to $\{111\}_\gamma$ twinning [29, 40–42], and that further increasing the strain leads to the onset of the $\gamma \rightarrow \epsilon$ martensitic transformation which further refines the original grains by the formation of intragranular ϵ-martensite platelets and their intersection. Within layer 1, it is found that the density of intergranular deformation bands increases towards the contacting surface due to the increasing strain.

4.1.2. Layer 2

Layer 2 is a transition region of severe plastic deformation which shows increased microstructural refinement as the surface is approached (Figs. 6 to 8). It starts at depths $\gtrsim 1$ and 2 μm following testing at 20 ^{o}C and 250 ^{o}C respectively, and then merges into layer 1. The grain refinement in this region is so extensive that the original grain boundaries become indistinguishable (Figs. 6 to 8). Additionally, the high density of ϵ-martensite platelets and their intersection heavily refines the microstructure (Figs. 6 to 8). The ϵ-martensite phase is heavily flawed with (0001) stacking faults (Fig. 8 (observed as fine closely spaced parallel striations)) due to both the nature of the $\gamma \rightarrow \epsilon$ transformation and the extensive strain imposed by the sliding contact deformation [28, 29, 36]. It is likely that as the surface is approached the increasing strain is first accommodated by an increasing fraction of $\gamma \rightarrow \epsilon$ transformation. At this stage, the development of ϵ-martensite lamellae and networks makes the accommodation of strain particularly difficult in the ϵ-martensite phase therefore, it is likely that deformation is principally accommodated by further transformation of the γ-phase. However, at some point within layer 2, the γ-phase will have fully transformed to the hcp ϵ-phase (Fig. 7) and further strain will have to be accommodated by either the twinning and/or dislocation slip of this phase. Given the low SFE of the ϵ-martensite phase, it is postulated that deformation will principally be accommodated by twinning (Fig. 8) of the ϵ-martensite which further reduces the effective grain size within this region of the TAM. Twinning is extensively observed in pure hcp ϵ-cobalt

during plastic deformation [29,43–45], even within nanoscale grains [29,45], due to its low stacking fault energy (27 ± 4 mJ/m^2) [46,47], therefore it is very likely to have occurred in these Stellite 6 samples.

4.1.3. Layer 3

Layer 3 is defined as the region of TAM within $\lesssim 1$ and 2 μm of the surface following testing at 20 ^{o}C and 250 ^{o}C respectively, and is characterized by predominantly equiaxed nanoscale grains composed entirely of ϵ-martensite (as identified by the SAD (Fig. 9)) < 100 nm in size (Figs. 8 and 9). These nanocrystalline grains are heavily flawed with (0001) stacking faults of various orientations and Moiré fringes are also observed (Fig. 9). In layer 3, it is probable that basal and prism dislocation slip become the dominant mechanism of strain accommodation within the ϵ-Co phase. It is postulated that further grain refinement is achieved via subdivision due to the slip of dislocations which permits the generation of a largely equiaxed nanocrystalline grain structure (Figs. 8 and 9). It is also suggested that the misorientation between subdivided grains is increased by further dislocation slip on these primary slip systems. There exists a high degree of grain boundary disorder, presumably due to dislocation activity as revealed by TEM (Figs. 8 and 9) and the lack of clearly defined grain boundaries suggests that grain boundary mediated deformation (e.g. grain rotation and grain boundary sliding) must be confined to the highest strained regions of layer 3 [29]. Grain boundary rotation and slip and the increased intergranular misorientation caused by dislocation slip could cause the alignment of the primary slip systems parallel to the direction of shear identified in XRD (Fig. 5). The alignment of these primary slip systems has previously been reported in pure cobalt [48–50] and Stellite type alloys [51–53]. These planes are the planes of lowest friction during sliding and are believed to readily accommodate deformation through shear [48–53]. However, this preferred orientation may also be a result of the heavily flawed nature of the ϵ-Co phase. Dynamic recrystallisation is believed not to be operative as there appears to be no nucleation/growth period and layer 3 is not composed of defect-free grains with clearly defined boundaries typically observed in dynamically recrystallised

materials (Figs. 8 and 9). However, continuous dynamic recrystallization is believed to be operative because a lineage with the previous deformation structures is retained during microstructural evolution. Similar observations have been made in a comparable Co-based alloy system [34].

The transition between layer 2 and 3 can be regarded as the region within which dislocation slip replaces twinning of the ϵ phase as the principal mode of deformation. Dislocation activity has been observed in these regions via TEM (Figs. 8 and 9). Thus, in accord with various other studies [29,45], it is hypothesised that dislocation slip becomes operative principally in the form of basal ($\langle 11\bar{2}0\rangle(0001)$) and prismatic ($\langle 11\bar{2}0\rangle\{10\bar{1}0\}$) slip. This concurs with Rietveld analysis which showed that the ϵ-phase had a c/a ratio ~ 1.615 which is close to ideal (1.633), so it is expected that both these primary slip systems are active [39,54]. However, cracking or void formation is not generally apparent in the highly strained nanocrystalline region (Figs. 8 and 9) therefore, either twinning or $\langle c+a\rangle$ dislocation slip must also be operative in order to satisfy the von Mises requirement for homogenous deformation [39,55]. It is proposed that the shift in the dominant deformation mechanism from twinning to dislocation slip of the ϵ-martensite phase can be explained in terms of the reduction in the effective grain size as the sample surface is approached. The critical resolved shear stress for twinning is known to increase as the effective grain size is reduced [28,29,56,57]. The transition in the dominant deformation mode occurs when the critical resolved shear stress for dislocation slip falls below that for twinning as a result of a refinement in the effective grain size [29]. This shift in the mechanisms of strain accommodation has been reported previously in several hcp materials [58–60].

4.1.4. Influence of test temperature on deformation features

Although the general microstructural features and deformation mechanisms of the three layers discussed above are representative of the observations made on samples tested at 20 ^{o}C and 250 ^{o}C, some differences are observed between the two test temperatures. For example, the extent of $\gamma \rightarrow \epsilon$ transformation observed in EBSD (Fig. 7) and XRD (Fig. 5) and the depths to which different

deformation mechanisms operate beneath the contacting surface. One factor which may be responsible for some of the differences observed in matrix deformation behaviour with respect to temperature is the temperature dependent nature of the SFE of the γ- and ϵ-phases in Stellite 6. Several other studies attribute a temperature dependent reduction in the fraction of $\gamma \rightarrow \epsilon$ transformation during sliding experiments conducted in air on Stellite alloys to a change in the SFE [61,62]. Whilst currently data do not exist on the SFE of the specific matrix phase compositions in Stellite 6, the temperature dependent nature of both γ- and ϵ-Co has been demonstrated in pure Co [46,47] and other Co-based binary and tertiary alloys [47,63]. It is therefore hypothesised that temperature dependence of the SFE for both the γ- and ϵ-phases in Stellite 6 may affect the critical strains (and therefore subsurface locations) of the different deformation mechanisms as well as the fraction of $\gamma \rightarrow \epsilon$ SIMT.

A temperature dependent increase in wear has previously been reported in Stellite alloys during sliding in air over the temperature ranges investigated in this work (20-250 ^{o}C) despite the potential tribological benefits of oxide glaze layers which may form at higher temperatures [61,62,64]. In these instances, the increased wear with respect to increasing temperature over this temperature range was attributed to an increase in the SFE of the matrix and a reduction in the fraction of SIMT and therefore work hardenability [61,62]. Whilst these studies agree with the general trends in material removal observed in this work, the $\sim$ 16.5 - 38.7 times increase in volume loss during sliding in autoclave conditions far exceeds those observed during in air sliding. Although important, it is clear that the temperature dependent nature of SFE does not solely account for the observed increase in wear and therefore, other phenomena must also significantly influence the rate of material removal with increasing test temperature which is explored further in the section on corrosion.

4.1.5. The role of carbide precipitates

In Stellite 6, detailed characterisation of the matrix-carbide interaction within the TAM has shown that the M_7C_3 precipitates effectively reduce plastic flow by

acting as rigid bodies which constrain the matrix and homogenise deformation. The loading conditions imposed by sliding can be described by simple shear and compression [65], but the presence of the M_7C_3 phase assists in the generation of multiaxial stress states within the matrix. This promotes the activation of different crystallographic deformation systems (faulting on the (111) planes and slip system activation) thus promoting potent matrix work hardening. It is suggested that the M_7C_3 precipitates within the TAM can remain underpinned by the matrix regions subjected to lower strains such that they act to reduce and partially equalize/homogenise the strain gradient within the surrounding matrix closer to the contacting surface. This matrix-carbide interaction significantly stabilises the TAM, contributes to work hardening and helps confine severe plastic deformation within close proximity to the contacting surface.

In summary, the characteristics of each of these layers is summarised in Table 3.

Table 3: Summary of the dominant mechanisms governing the subsurface microstructural evolution beneath the contacting surface of Stellite 6 in response to sliding in lithiated water.

Deformation layer	Relative strain	ϵ phase (hcp)	γ phase (fcc)
3	high	• Grain boundary sliding and rotation • Basal and prism plane alignment • Nanocrystal formation • Grain subdivision by dislocation activity • Basal ($\langle 11\bar{2}0\rangle(0001)$) and prismatic dislocation slip ($\langle 11\bar{2}0\rangle\{10\bar{1}0\}$)	
2	medium	• Basal ($\langle 11\bar{2}0\rangle(0001)$) and prismatic dislocation slip ($\langle 11\bar{2}0\rangle\{10\bar{1}0\}$) • Twinning • Glide of (0001) stacking faults • Basal and pyramidal dislcoations	• $\gamma \rightarrow \epsilon$ Transformation (complete transformation)
1	low	• Twinning • Glide of (0001) stacking faults • Basal and pyramidal dislcoations	• $\gamma \rightarrow \epsilon$ Transformation • $\{111\}$ Twinning • Glide of 111 Stacking faults • Dislocation slip on the 111 planes

4.2. Mechanical removal of material

Macro/micro-scale material transfer, adhesion and extrusion via ratchetting at the contacting surfaces are rarely observed at either of the test temperatures. By characterising the deformation microstructures beneath the contacting surface in

such detail, significant insights have been gained into understanding why Stellite 6 remains so resistant to plasticity dominated wear, adhesion, and material transfer. In related alloys, micro/macro scale shear localisation phenomena and localised instabilities are generally believed to be precursors to material fracture and transfer events during sliding [65–69]. However, the deformation structures observed at any given depth below the contacting surface of Stellite 6 appear to have resulted in a largely homogenous accommodation of strain on the micro/macro scale and any heterogeneous deformation features are largely retained within the top 2 μm (Figs. 8 and 9). This resistance to both the generation of inhomogeneous deformation structures and shear localisation phenomena could well be an important reason why material transfer events and extruded slivers of material are rarely observed at the contacting surface of Stellite 6. It should also be noted that the presence of a corrosion product at the contacting surface (Fig. 10) will also limit material transfer events.

The principal mechanical degradation mechanisms of Stellite 6 in the present self-mated contact conditions appear to occur via material removal on the nanoscale (often termed nanowear). Despite the differences observed between the two different test temperatures, the previous sections have shown that the subsurface deformation mechanisms and structures within the TAM are generally similar following testing at 20 ^{o}C and 250 ^{o}C. With the exception of the occasional carbide fracture and pull-out (Fig. 4), detailed top-surface and cross-sectional investigations of the TAM have provided no evidence to suggest that macro/micro-scale wear mechanisms are the principal modes of degradation (Figs. 6 to 8). Any evidence of microscale subsurface localisation, microstructural instabilities, mechanical mixing, and the embedding of oxides was relatively infrequent and generally confined within the uppermost regions of layer 3 when investigated on the nanoscale via TEM at both testing temperatures. In light of the above, material detachment is most probably associated with the uppermost region of layer 3 and principally occurs on the nanoscale via the direct removal of nano-sized elements from the sample surface and not typically by macro/micro-scale subsurface rupture as is hypothesised in more conventional wear theories [4]. The following sections aim

to elaborate on the potential mechanisms of nanoscale material removal.

4.3. Oxidation and tribocorrosion in lithiated water

The previous sections have shown that degradation is principally confined to the nanoscale removal of material from uppermost region of the nano-crystalline layer. Therefore, the oxidative behaviour at the contacting surface of Stellite 6 and its temperature dependence must also be significant to degradation during sliding contact in lithiated water. In related Stellite alloys and tribochemical environments (e.g. 0.5M H_2SO_4), several studies exist which propose that tribocorrosion is the principal cause of degradation during sliding contact tests in different aqueous environments where passivating behaviour is observed [8–14, 70]. Stellite 6 is known to exhibit passivating behaviour in lithiated water at both 20 ^oC and 250 ^oC and thin corrosion films composed of CoO and Cr_2O_3 are known to develop [24–26]. During self-mated sliding contact in a lithiated water environment at 20 ^oC and 250 ^oC, Ratia et al. [21, 22] suggest that the principal factor governing degradation is the repeated removal and regrowth of a passive oxide film on Stellite 6 by the application of a mechanical stimulus (i.e. wear enhanced corrosion - the corrosion of depassivated metal). Tribocorrosion of the carbide phase, i.e. the amount of material removed during a sliding contact depassivation/passivation cycle, is potentially related to the mechanism and kinetics of oxide film formation over the carbide surface. Hocking et al. [26] have shown that in lithiated high temperature water, an oxide film forms over the carbide but with a lower thickness than over the matrix ($\sim$ 40 %). This concurs with other studies which suggest that the Co-rich matrix corrodes faster than the carbide phase [71, 72].

In the present work, the passivating behaviour of Stellite 6 was confirmed and TEM revealed a thin (10 - 20 nm) passive oxide layer at the contacting surface which is principally composed of Co and a smaller fraction of Cr (Fig. 10) following testing at 250 ^oC. This observation agrees with various earlier studies [24–26]. For example, the X-ray photoelectron spectroscopy study by McIntyre et al. [25] who

identified a 10 to 15 nm thick passive film involving primarily CoO and Cr_2O_3 when Stellite 6 was tested in water of pH 10 at 285 ^{o}C during short term exposure (168 h). Whilst, the passive film observed in Fig. 10 could be affected by the time spent in lithiated water at various temperatures during the autoclave cool down period following testing at 250 ^{o}C. Further growth of the passive film and/or metal dissolution is possible during this period; however it is likely that the extent of growth would be small as the kinetics must slow down as the temperature falls. Additionally, fast passive film growth is expected on a depassivated surface (wear induced) which subsequently slows once a stable film forms - especially at low temperatures [13].

4.4. Synergistic degradation effects in lithiated water

It is clear that the passivating behaviour of Stellite 6 is fundamentally important to degradation via tribocorrosion during sliding in lithiated water [9,21,22]. However, the mechanisms of tribocorrosion (corrosion enhanced wear and wear enhanced corrosion) leading to the nanoscale removal of material are less well understood, and the role of passivation needs to be integrated with subsurface mechanical deformation, mechanical mixing and three-body sliding abrasion effects when evaluating nanoscale material detachment. Based on the findings presented in this work, it seems likely that degradation involves a complex interaction of both mechanical deformation and chemical phenomena. These collectively result in the detachment of predominantly nanoscale particulates composed of oxidised material which may also contain a fraction of metallic and/or mixed metal plus oxidised material at the point of detachment. Regardless, the wear enhanced corrosion mechanism (i.e. the corrosion of depassivated metal) which has previously been described in the literature still seems to be generally applicable to the self-mated sliding of Stellite 6 in lithiated water, despite the fact it is almost certainly an oversimplification of the tribocorrosion phenomena occurring in the present investigation [9,21,22].

Temperature dependent variation in the oxidative reactions and passivating behaviour occurring at the contacting surface of Stellite 6 are likely to influence the plastic strain accumulation and the deformation characteristics and microstructures within the subsurface (Figs. 6 to 9). It is postulated that the increase in the passive oxide thickness observed at 250 ^{o}C may lead to increased strain during sliding. This is one factor which could account for the increased deformation observed at any given depth following testing at 250 ^{o}C (Figs. 6 to 9). This concurs with Maldonado et al. [9] who showed that increased passivation on Stellite type alloys increases the strain induced during sliding. In light of the above, it is suggested that the differences observed in the deformation induced subsurface microstructure between the different test temperatures (Figs. 6 to 9) will influence the passive behaviour at the contact. Likewise, the extent of passivation at a given temperature will influence the deformation mechanisms and subsurface strains. The rate of passivation and extent of subsurface deformation are closely coupled to one another and are both influenced by temperature; this interaction between chemical and mechanical phenomena may influence the rate of material removal from the surface.

It is possible that metal dissolution and passivation reactions at the contacting surface may enhance the wear of the nanocrystalline layer [9, 15, 73–76]. Given the matrix deformation mechanisms identified within the nanocrystaline layer, it is possible that oxidation/passivation, molecular absorption and/or dissolution may influence near surface mechanical properties and intergranular bonding which will affect the removal of nanoscale particulates from the surface. Several studies [9, 76] suggest that passive films influence the deformation characteristics within nanocrystalline layers possibly by: (i) acting as a source of dislocations and/or other deformation structures due to a potential mismatch in elastic properties between the passive film and underlying material, (ii) manipulating the composition and therefore SFE of the metallic material directly beneath the passive film which alters the critical strains for deformation, and (iii) obstructing the free surface therefore hindering dislocation annihilation. Increased defect densities due to the presence of a passive layer will promote increased continuous dynamic

recrystallization and the generation of increasingly smaller grains beneath the subsurface (Figs. 8 and 9) which may influence the nanoscale removal of material. However, it is recognised that these phenomena are fundamentally dependent on classical (dislocation mediated) deformation mechanisms which may be less significant to strain accommodation in the regions directly adjacent to the interface. Grain boundary sliding and rotation has been highlighted as a possible deformation mode in the highest strained regions of the nanocrystalline layer; therefore the potential chemical manipulation/modification of grain boundaries due to passivation may be significant in the removal of nanoscale particulates.

TEM has shown that nanolayers may develop at the contacting surface in the form of < 20 nm thick mechanically mixed nanolayer/tribofilm within which almost no microstructural features are clearly distinguishable (Fig. 11). In this particular instance, the tribofilm is generated as matrix material is forced to plastically flow over the top of an M_7C_3 carbide (Fig. 11). However, such features have also been observed over the matrix phase and do not cover the entirety of the contacting surface. Regardless, these nanolayers have clearly accommodated large strains. It is probable that nanoscale mechanical mixing within the autoclave environment causes a compositional change within the tribofilm (Fig. 11); this is most probably due to oxidation, metal dissolution and/or oxide embedding. The formation of this tribofilm may account for the mottled variation in contrast that is observed across both the carbide and matrix phases (Fig. 4). It is hypothesised that this nanoscale mechanical mixing and interaction with the test environment may be partially responsible for material detachment and possibly contribute to the higher rates of wear at 250 ^{o}C. Moreover, a compromised ability to retain a tribofilm due to environmental changes including increased passivation at elevated temperature (250 ^{o}C) may be a factor which contributes to the increased wear observed at 250 ^{o}C as well as the difference in subsurface deformation. It is not definitively clear how these nanolayers become detached or degrade; however discontinuities have been observed at the interface between the nanolayer and the bulk material (Fig. 11) which suggests fracture after extrusion via plastic ratchetting may be important. Additionally, the extent of chemical degradation/oxidation during the mechanical

mixing of these nanolayers prior to their detachment or degradation still remains much debated. Whilst the classical wear enhanced corrosion mechanism which involves the corrosion of depassivated metal is still relevant [9,21,22], such mechanisms do not account for the formation of mechanically mixed nanolayers on the contacting surface. Thus, the term "corrosion enhanced nanowear" seems to be a more fitting way of describing degradation in the instance where nanolayers are present. These nanocrystalline tribofilms readily accommodate high strains possibly by grain boundary mediated deformation mechanisms (e.g. grain boundary slip and rotation) and crystallographic slip. Therefore, the formation of such tribofilms may partially account for the preferred orientation of the primary slip systems observed in XRD (Fig. 5). These planes are reported to be the planes of lowest friction which readily accommodate deformation through shear [48–53].

The scratching and scoring observed on the contacting surface (Figs. 3 and 4) are likely to be influenced by debris particles/agglomerates partially retained within the sliding contact [9]. The increased plastic disturbance and surface roughening caused by abrasive debris within the sliding contact unquestionably promotes nanoscale material removal, possibly by micro-cutting in some instances given that notable prow formation is not frequently observed (Fig. 4) [9]. One source of abrasive particles comes from the carbides, and several micro and nanoscale abrasion marks can be directly traced back to the locations where carbide pull-out has occurred (Fig. 4). The M_7C_3 precipitates are largely equiaxed in as-received HIPed Stellite 6 (Fig. 1) therefore, the high aspect ratio carbides observed at the contacting surface (Figs. 8, 11 and 12) must be generated by the wear of carbides which are effectively constrained at the sliding interface by the surrounding matrix. It is postulated that carbide pull-out may occur when the carbide reaches a critical thickness where carbide fracture may occur (Figs. 4 and 12) and/or, the combined matrix-carbide interaction is no longer an effective barrier to extensive plastic flow (Fig. 4). For example, the vertical crack in the carbide shown in Fig. 12 most probably occurs when it is critically thinned to a point where it can no longer support the loads imposed during sliding.

The tribologically affected surface is considerably rougher following testing at

250 ^{o}C (Figs. 3 and 4) and estimates of the average maximum wear track depth have been calculated to be $\sim$ 1.7 and 8.8 μm following testing at 20 ^{o}C and 250 ^{o}C respectively. This increase in surface roughness following elevated temperature testing can most probably be related to the average maximum wear depths and the scale of the microstructural features. The size of the M_7C_3 carbides are $\sim$ 1 - 4 μm with an average spacing of $\sim$ 2 - 3 μm between them. Upon comparing the microstructural scale and distribution of the carbides with the average maximum wear depths, it is clear that a higher fraction of carbides (or fragments of carbides) will be released during testing at 250 ^{o}C which subsequently generates a rougher surface.

Another source of nanoscale abrasive debris particles comes from the detachment of oxidised material and possibly work hardened matrix and/or mechanically mixed metal plus oxide. These nanoscale abrasive particles may oxidise further and agglomerate during sliding. The debris particles and agglomerates reportedly get bigger with increasing test temperature [21]. The larger fraction of debris contained within the sliding contact at any given time during testing at 250 ^{o}C increases the likelihood of particle agglomeration prior to ejection from the sliding contact; this may be a factor which contributes to the deeper abrasion marks and increased three-body sliding abrasion observed at 250 ^{o}C.

5. Conclusions

- The tribologically affected material beneath the sliding surface is subject to a deformation gradient where the highest strains are generated at the contacting surface.
- In the early stages of plastic deformation (furthest from the contacting surface), strain is principally accommodated by the complete deformation induced martensitic transformation of the γ-phase to ϵ-martensite. As the sample surface is approached, this ϵ-martensite phase accommodates further strain via twinning and basal and prismatic dislocation slip. In the highest strained regions directly adjacent to the contacting surface, the ϵ-martensite subsurface microstructure is nanocrystalline.
- Stellite 6 is highly resistant to plastic strain localisation phenomena due to an ability to sustain a sufficient strain hardening rate (continued defect storage at high strains) which prevents the accumulation of large strains in localised regions.
- It is proposed that the synergistic effect of the chemical manipulation of the near surface due to passivating behaviour and mechanical stimulation by sliding contact results in the removal of nanoscale particles from the contacting surface which may also cause further nanoscale degradation via three-body abrasion.
- The detachment of nanoscale particulates cannot be attributed to a single phenomenon; moreover, the unique subsurface deformation characteristics exhibited by Stellite 6 suppress material removal to the nanoscale where chemical oxidative reactions and other tribochemical interactions are capable of greatly influencing material detachment during sliding.
- A synergistic temperature dependent increase in corrosion rate and stacking fault energy principally account for the increased wear rates observed at 250 ^{o}C. However, the rate of corrosion is believed to be the dominant factor

influencing wear. These factors affect degradation through the modification of: mechanical deformation characteristics, the extent of corrosion enhanced wear and/or wear enhanced corrosion, the amount of nanoscale mechanical mixing, the frictional state of the contact, the amount of material detachment, and the degree of three-body abrasion. The amalgamation of these various factors is believed to result in the $\sim$ 16 - 39 times increase in material removal when the test temperature is increased from 20 to 250 ^{o}C.

Acknowledgements

The authors gratefully acknowledge funding from Rolls-Royce plc. M.J. Carrington also acknowledges funding from the Faculty of Engineering, University of Nottingham in support of a PhD studentship. The authors thank the Nanoscale and Microscale Research Centre (nmRC) for providing access to instrumentation. Access to the JEOL 7100F FEG-SEM was supported by the Engineering and Physical Sciences Research Council (EPSRC) [under grant EP/L022494/1] and the University of Nottingham. The authors also wish to thank Dr. Geoff West of the Warwick Manufacturing Group (WMG) at the University of Warwick for his technical assistance concerning TEM and TEM sample preparation.

REFERENCES

[1] H. Ocken. Reducing the cobalt inventory in light water reactors. *Nuclear Technology*, 68(1):18–28, 1985.

[2] H. Ocken. The galling wear resistance of new iron-base hardfacing alloys: a comparison with established cobalt-and nickel-base alloys. *Surface and Coatings Technology*, 76:456–461, 1995.

[3] B.G. Mellor. *Surface coatings for protection against wear*. Woodhead Publishing, 2006.

[4] I. Hutchings and P. Shipway. *Tribology: friction and wear of engineering materials*. Butterworth-Heinemann, 2017.

[5] H.V. Atkinson and B.A. Rickinson. *Hot isostatic processing*. Springer, 1991.

[6] E.K. Ohriner, E.P. Whelan, T. Wada, and H. Ocken. Cobalt-free, iron-base hardfacing alloys, 1989. US Patent 4803045.

[7] P. Crook and R.D. Zordan. Nuclear grade steels, 1987. US Patent 4,643,767.

[8] W.J. Chitty, J.P. Vernot, and N.P. Areva. Tribocorrosion issues in nuclear power generation. In *Tribocorrosion of Passive Metals and Coatings*, pages 424–440. Elsevier, 2011.

[9] S. Guadalupe Maldonado, S. Mischler, M. Cantoni, W.J. Chitty, C. Falcand, and D. Hertz. Mechanical and chemical mechanisms in the tribocorrosion of a Stellite type alloy. *Wear*, 308(1-2):213–221, 2013.

[10] S. Guadalupe, S. Cao, M. Cantoni, W.J. Chitty, C. Falcand, and S. Mischler. Applicability of a recently proposed tribocorrosion model to CoCr alloys with different carbides content. *Wear*, 376-377:203–211, 2017.

[11] D. Kaczorowski and J.P. Vernot. Wear problems in nuclear industry. *Tribology International*, 39(10):1286–1293, 2006.

[12] E. Lemaire and M. Le Calvar. Evidence of tribocorrosion wear in pressurized water reactors. *Wear*, 249(5-6):338–344, 2001.

[13] S. Xu, I.L. Kondratova, N. Arbeau, W. Cook, and D.H. Lister. Corrosion of UNS R30006 in high-temperature water under intermittent mechanical contact. *Corrosion*, 61(5):444–451, 2005.

[14] V. Iordache, F. Wenger, P Ponthiaux, A Ambard, J Peybernès, and J Vallory. Comparison between tribocorrosion mechanisms of Stellite 6 and Zircaloy 4 in LiOH-H_3BO_3 solutions. In *Passivation of Metals and Semiconductors, and Properties of Thin Oxide Layers*, pages 495 – 500. Elsevier Science, 2006.

[15] A.I Muñoz and N. Espallargas. Tribocorrosion mechanisms in sliding contacts. In *Tribocorrosion of passive metals and coatings*, pages 118–152. Elsevier, 2011.

[16] C. Zhao, D. Stewart, J. Jiang, and F.P.E. Dunne. A comparative assessment of iron and cobalt-based hard-facing alloy deformation using HR-EBSD and HR-DIC. *Acta Materialia*, 159:173–186, 2018.

[17] PWR primary water chemistry guidelines: Volume 1, revision 4. Technical report, Electric Power Research Inst., 1999.

[18] R.A. Young. *The rietveld method*, volume 6. Oxford University Press, 1993.

[19] R.W. Cheary and A. Coelho. A fundamental parameters approach to X-ray line-profile fitting. *Journal of Applied Crystallography*, 25(2):109–121, 1992.

[20] R.W. Cheary, A.A. Coelho, and J.P. Cline. Fundamental parameters line profile fitting in laboratory diffractometers. *Journal of Research of the National Institute of Standards and Technology*, 109(1):1, 2004.

[21] V.L. Ratia, D. Zhang, M.J. Carrington, J.L. Daure, D.G. McCartney, P.H. Shipway, and D.A. Stewart. The effect of temperature on sliding wear of self-mated HIPed Stellite 6 in a simulated PWR water environment. *Wear*, 420:215–225, 2019.

[22] V.L. Ratia, D. Zhang, M.J. Carrington, J.L. Daure, P.H. McCartney, D.G.and Shipway, and D.A. Stewart. Comparison of the sliding wear behaviour of self-mated HIPed Stellite 3 and Stellite 6 in a simulated PWR water environment. *Wear*, 426:1222–1232, 2019.

[23] B.D Cullity. *Elements of X-ray Diffraction*. Addison-Wesley Publishing, 1956.

[24] N.K. Taylor and I. Armson. Corrosion product release from stellites and stainless steel in high pressure, high temperature lithiated water. In *Water chemistry of nuclear reactor systems 3: Proceedings of an international conference*, pages 141–151, London, 1983. British Nuclear Society.

[25] N.S. McIntyre, D. Zetaruk, and E.V. Murphy. X-Ray photoelectron spectroscopic study of the aqueous oxidation of stellite-6 alloy. *Surface and Interface Analysis*, 1(4):105–110, 1979.

[26] W.H. Hocking, F.W. Stanchell, E. McAlpine, and D.H. Lister. Mechanisms of corrosion of Stellite-6 in lithiated high temperature water. *Corrosion Science*, 25(7):531–557, 1985.

[27] J.A. Greenwood and J.B.P. Williamson. Contact of nominally flat surfaces. *Proceedings of the Royal Society of London. Series A. Mathematical and Physical Sciences*, 295(1442):300–319, 1966.

[28] X. Wu, N. Tao, Y. Hong, J. Lu, and K. Lu. $\gamma \rightarrow \epsilon$ martensite transformation and twinning deformation in fcc cobalt during surface mechanical attrition treatment. *Scripta Materialia*, 52(7):547–551, 2005.

[29] X. Wu, N. Tao, Y. Hong, G. Liu, B. Xu, J. Lu, and K. Lu. Strain-induced grain refinement of cobalt during surface mechanical attrition treatment. *Acta Materialia*, 53(3):681–691, 2005.

[30] M.J. Bibby and J.G. Parr. The $\alpha \rightarrow \epsilon$ transformation in polycrystalline cobalt. Technical report, Alberta Univ. Edmonton, 1963.

[31] H. Bibring, F. Sebilleau, and C.J. Bückle. The kinetics and morphology of the allotropic transformation of cobalt. *Journal of the Institute Metals*, 87(3):71–76, 1958.

[32] *Cobalt Monograph*. Centre d'Information du Cobalt, Brussels, 1960.

[33] R. Ahmed and H. de Villiers-Lovelock. Friction and wear of cobalt-base alloys. In *Friction, Lubrication, and Wear Technology*. ASM International, 2017.

[34] R. Büscher and A. Fischer. The pathways of dynamic recrystallization in all-metal hip joints. *Wear*, 259(7-12):887–897, 2005.

[35] R.T. Smith, T. Lolla, D. Gandy, L. Wu, G. Faria, A.J. Ramirez, S.S. Babu, and P.M. Anderson. In situ X-ray diffraction analysis of strain-induced transformations in Fe- and Co-base hardfacing alloys. *Scripta Materialia*, 98:60–63, 2015.

[36] G.B. Olson and M. Cohen. A general mechanism of martensitic nucleation: Part I. general concepts and the FCC $\rightarrow$ HCP transformation. *Metallurgical Transactions A*, 7(12):1897–1904, 1976.

[37] H. Fujita and S. Ueda. Stacking faults and fcc (γ) $\rightarrow$ hcp (ϵ) transformation in 188-type stainless steel. *Acta Metallurgica*, 20(5):759–767, 1972.

[38] Y. Koizumi, S. Suzuki, K. Yamanaka, B. Lee, K. Sato, Y. Li, S. Kurosu, H. Matsumoto, and A. Chiba. Strain-induced martensitic transformation near twin boundaries in a biomedical Co–Cr–Mo alloy with negative stacking fault energy. *Acta Materialia*, 61(5):1648–1661, 2013.

[39] Y. Cao, S. Ni, X. Liao, M. Song, and Y. Zhu. Structural evolutions of metallic materials processed by severe plastic deformation. *Materials Science and Engineering: R: Reports*, 133:1–59, 2018.

[40] N.R. Tao, X.L. Wu, M.L. Sui, J. Lu, and K. Lu. Grain refinement at the nanoscale via mechanical twinning and dislocation interaction in a nickel-based alloy. *Journal of Materials Research*, 19(6):1623–1629, 2004.

[41] H.W. Zhang, Z.K. Hei, G. Liu, J. Lu, and K. Lu. Formation of nanostructured surface layer on AISI 304 stainless steel by means of surface mechanical attrition treatment. *Acta Materialia*, 51(7):1871–1881, 2003.

[42] I. Karaman, H. Sehitoglu, Y.I. Chumlyakov, and H.J. Maier. The deformation of low-stacking-fault-energy austenitic steels. *The Journal of The Minerals, Metals & Materials Society*, 54(7):31–37, 2002.

[43] X.Y. Zhang, Y.T. Zhu, and Q. Liu. Deformation twinning in polycrystalline Co during room temperature dynamic plastic deformation. *Scripta Materialia*, 63(4):387–390, 2010.

[44] Y.T. Zhu, X.Y. Zhang, and Q. Liu. Observation of twins in polycrystalline cobalt containing face-center-cubic and hexagonal-close-packed phases. *Materials Science and Engineering: A*, 528(28):8145–8149, 2011.

[45] K. Edalati, S. Toh, M. Arita, M. Watanabe, and Z. Horita. High-pressure torsion of pure cobalt: hcp-fcc phase transformations and twinning during severe plastic deformation. *Applied Physics Letters*, 102(18):181902, 2013.

[46] A. Korner and H.P. Karnthaler. Weak-beam study of glide dislocations in hcp cobalt. *Philosophical Magazine A*, 48(3):469–477, 1983.

[47] L. Rémy, A. Pineau, and B. Thomas. Temperature dependence of stacking fault energy in close-packed metals and alloys. *Materials Science and Engineering*, 36(1):47–63, 1978.

[48] W.J. Huppmann and M.A. Clegg. The tribological behavior of polycrystalline cobalt as related to crystallographic texture and structure. *ASLE Transactions*, 16(2):107–114, 1973.

[49] M. Barquins and R. Courtel. Plastic deformation by friction of some hexagonal single crystals: Be, Co, Zn, Cd. *ASLE Transactions*, 14(2):81–89, 1971.

[50] D.R. Wheeler and D.H. Buckley. Texturing in metals as a result of sliding. *Wear*, 33(1):65–74, 1975.

[51] D.H.E. Persson, S. Jacobson, and S. Hogmark. Antigalling and low friction properties of a laser processed Co-based material. *Journal of Laser Applications*, 15(2):115–119, 2003.

[52] D.H.E. Persson, E. Coronel, S. Jacobson, and S. Hogmark. Surface analysis of laser cladded Stellite exposed to self-mated high load dry sliding. *Wear*, 261(1):96–100, 2006.

[53] D.H.E. Persson, S. Jacobson, and S. Hogmark. Effect of temperature on friction and galling of laser processed Norem 02 and Stellite 21. *Wear*, 255(1-6):498–503, 2003.

[54] M.H. Yoo and C.T. Wei. Slip modes of hexagonal-close-packed metals. *Journal of Applied Physics*, 38(11):4317–4322, 1967.

[55] M.H. Yoo. Slip, twinning, and fracture in hexagonal close-packed metals. *Metallurgical Transactions A*, 12(3):409–418, 1981.

[56] M.A. Meyers, O. Vöhringer, and V.A. Lubarda. The onset of twinning in metals: a constitutive description. *Acta Materialia*, 49(19):4025–4039, 2001.

[57] Y.T. Zhu, X.Z. Liao, and X.L. Wu. Deformation twinning in nanocrystalline materials. *Progress in Materials Science*, 57(1):1–62, 2012.

[58] D.H. Shin, I. Kim, J. Kim, Y.S. Kim, and S.L. Semiatin. Microstructure development during equal-channel angular pressing of titanium. *Acta Materialia*, 51(4):983–996, 2003.

[59] K.Y. Zhu, A. Vassel, F. Brisset, K. Lu, and J. Lu. Nanostructure formation mechanism of α-titanium using SMAT. *Acta Materialia*, 52(14):4101–4110, 2004.

[60] W.S. Choi, H.S. Ryoo, S.K. Hwang, M.H. Kim, S.I. Kwun, and S.W. Chae. Microstructure evolution in Zr under equal channel angular pressing. *Metallurgical and Materials Transactions A*, 33(3):973, 2002.

[61] H. Kashani, A. Amadeh, and A. Ohadizadeh. Effect of temperature on the strain induced $\gamma \rightarrow \epsilon$ phase transformation in Stellite 21 during wear test. *Materials Science and Engineering: A*, 435:474–477, 2006.

[62] I. Radu, D.Y. Li, and R. Llewellyn. Tribological behavior of Stellite 21 modified with yttrium. *Wear*, 257(11):1154–1166, 2004.

[63] T. Ericsson. The temperature and concentration dependence of the stacking fault energy in the Co-Ni system. *Acta Metallurgica*, 14(7):853–865, 1966.

[64] F.H. Stott, C.W. Stevenson, and G.C. Wood. Friction and wear properties of Stellite 31 at temperatures from 293 to 1073 K. *Metals Technology*, 4(1):66–74, 1977.

[65] W.M. Rainforth, R. Stevens, and J. Nutting. Deformation structures induced by sliding contact. *Philosophical Magazine A*, 66(4):621–641, 1992.

[66] D.A. Rigney, L.H. Chen, M.G.S. Naylor, and A.R. Rosenfield. Wear processes in sliding systems. *Wear*, 100(1-3):195–219, 1984.

[67] R. Smith, M. Doran, D. Gandy, S. Babu, L. Wu, A.J. Ramirez, and P.M. Anderson. Development of a gall-resistant stainless-steel hardfacing alloy. *Materials & Design*, 143:38–48, 2018.

[68] S.M. Kuo and D.A. Rigney. Sliding behavior of aluminum. *Materials Science and Engineering: A*, 157(2):131–143, 1992.

[69] D.A. Rigney. Transfer, mixing and associated chemical and mechanical processes during the sliding of ductile materials. *Wear*, 245(1-2):1–9, 2000.

[70] S.G. Maldonado, S. Mischler, M. Cantoni, W.J. Chitty, C. Falcand, and D. Hertz. Mechanical and chemical mechanisms in the tribocorrosion of a Stellite type alloy. *Wear*, 308(1-2):213–221, 2013.

[71] G.N. Karimi, M.J. Carrington, J. Thomas, P.H. Shipway, D.A. Stewart, and T. Hussain. The role of microstructural development in the hydrothermal corrosion of cast and HIPed Stellite 6 analogues in simulated PWR conditions. *Corrosion Science*, 159:108141, 2019.

[72] G.N. Karimi, P.H. Shipway, D.A. Stewart, and T. Hussain. Corrosion of cast Stellite-3 analogue in simulated PWR conditions. *Corrosion Science*, 140:402–411, 2018.

[73] M. Favero, P. Stadelmann, and S. Mischler. Effect of the applied potential of the near surface microstructure of a 316L steel submitted to tribocorrosion in sulfuric acid. *Journal of Physics D: Applied Physics*, 39(15):3175, 2006.

[74] R. Büscher, G. Täger, W. Dudzinski, B. Gleising, M.A. Wimmer, and A. Fischer. Subsurface microstructure of metal-on-metal hip joints and its relationship to wear particle generation. *Journal of Biomedical Materials Research Part B: Applied Biomaterials*, 72(1):206–214, 2005.

[75] A. Bidiville, M. Favero, P. Stadelmann, and S. Mischler. Effect of surface chemistry on the mechanical response of metals in sliding tribocorrosion systems. *Wear*, 263(1-6):207–217, 2007.

[76] J. Perret, E. Boehm-Courjault, M. Cantoni, S. Mischler, A. Beaudouin, W. Chitty, and J.P. Vernot. EBSD, SEM and FIB characterisation of subsurface deformation during tribocorrosion of stainless steel in sulphuric acid. *Wear*, 269(5-6):383–393, 2010.

APPENDIX A.

PHASE IDENTIFICATION USING X-RAY DIFFRACTION

Fig. A-1 shows an X-ray diffractogram from the polished surface of as-received HIPed Stellite 6.

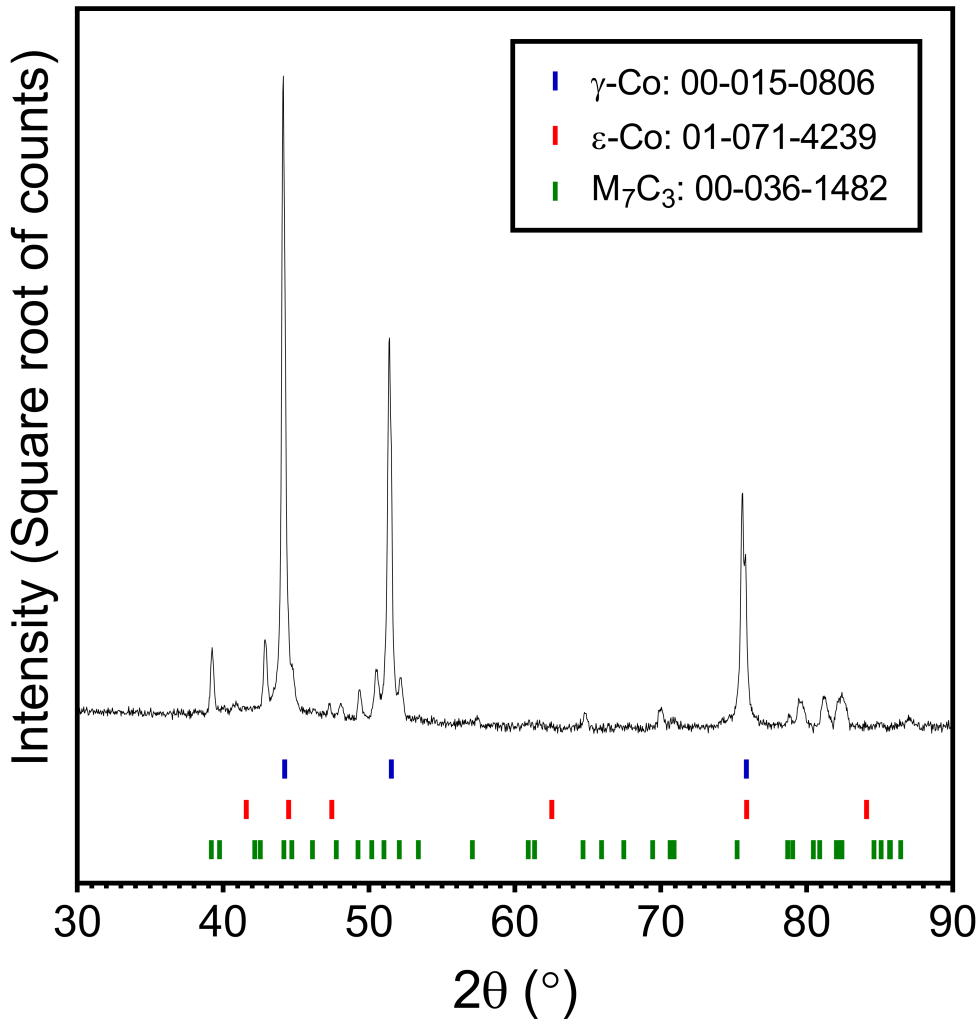

Figure A-1: XRD pattern obtained from the polished surface of the as-received, HIPed Stellite 6. The ICDD database files used to index the diffractogram is shown in the legend. Stellite 6 exhibits reflections for γ-Co (fcc), M_7C_3 and a very small fraction of ϵ-Co (hcp).

INDIVIDUAL PIN AND DISC WEAR

Table A-1 shows a breakdown of the individual pin and disc mass losses following autoclave testing at 20 ^{o}C and 250 ^{o}C.

Table A-1: The effect of test temperature on the individual components of pin and disc mass loss of Stellite 6 following 5 h autoclave sliding contact testing with a dead load of 4 kg. The errors have been reported as the standard error of the mean.

Test temperature (^{o}C)	**Pin mass loss (mg)**	**Disc mass loss (mg)**	**Total mass loss (mg)**
20	0.5±0.1	1.0±0.3	1.5±0.4
250	17.7±2.8	19.4±3.9	37.0±1.9

List of Figures

1 BSE-SEM channelling contrast micrographs (a and b) and both EBSD-derived phase (c) and IPFZ (d) maps of HIPed Stellite 6. (a) and (b) show M_7C_3 carbides (darkest contrast) and cobalt-based matrix grains with annealing twins. (c) shows M_7C_3 carbides (yellow) surrounded by a fcc Co-based solid solution matrix (blue (γ-SS)) and a small fraction of a hcp Co-based solid solution (grains) and ϵ-martensite laths (red (ϵ-SS/Ms)). (d) depicts the same region shown in (c) and shows matrix grains with high angle annealing twins. . . 11

2 Graph showing the effect of autoclave test temperature on the mass and volume loss following 5 h sliding contact testing with a 4 kg dead load. The bars represent mean values and the error bars represent the minimum and maximum values of combined pin and disc wear. Three tests were conducted at 20 ^{o}C and six at 250 ^{o}C . . 12

3 Stereoscope optical micrographs of Stellite 6 disc ((a) and (b)) and pin ((c) and (d)) tribologically/chemically affected surfaces following sliding contact autoclave tests at 20 ((a) and (c)) and 250 ^{o}C ((b) and (d)). 14

4 Plan view BSE-SEM micrographs showing the microstructure of the tribologically/chemically affected surface of Stellite 6 disc samples after sliding contact tests in an autoclave environment at 20 ^{o}C (a and c) and 250 ^{o}C (b and d) for 5 hours. Sliding direction was horizontal on the image. Carbide pull-outs are indicated by red arrows. 15

5 XRD patterns from the polished surface of the as-received Stellite 6 (black) and from within the wear track of disc samples (following testing at 20 ^{o}C and 250 ^{o}C)(red). Patterns normalised to the reflection of maximum intensity. 17

6 Cross-sectional BSE-SEM channelling contrast micrographs of Stellite 6 taken from within the wear track of disc samples (parallel to the sliding direction) after testing at 20 ^{o}C (a, c) and 250 ^{o}C (b, d). M_7C_3 (dark contract) carbides are distributed in Co-rich matrix with traces of planar deformation structures. 18
7 EBSD derived phase maps ((a) and (b)), band contrast maps ((c) and (d)) and inverse pole figures ((e) and (f)) taken perpendicular to the sliding direction of HIPed Stellite 6 disc samples following autoclave sliding wear testing at 20 ((a), (c) and (e)) and 250 ^{o}C ((b), (d) and (f)). Regions which could not be indexed are shown in black. 20
8 Representative BF-STEM micrographs of Stellite 6 disc samples taken from within the wear track (parallel to the sliding direction) after testing at 20 ^{o}C (a, c) and 250 ^{o}C (b, d). Angular, micron sized M_7C_3 particles are visible within the highly faulted cobalt-rich matrix 21
9 Representative BF-TEM micrographs ((a) and (c)) and SADPs ((c) and (d)) from samples taken parallel to the direction of shear, showing the deformation structures directly beneath the contacting surface of Stellite 6 disc samples after exposure to sliding contact at 20 ^{o}C ((a) and (b)) and 250 ^{o}C ((c) and (d)). The SADPs, (b) and (d), index to hcp ϵ-Co and have been recorded from the regions marked with circles in (a) and (c) respectively. 22
10 (a) BF-STEM micrograph of a Stellite 6 disc sample taken parallel to the direction of shear following exposure to sliding contact at 250 ^{o}C. (b), (c) and (d) show EDX maps of the same region depicted in (a) and correspond to maps for O, Cr and Co respectively. 23
11 Micrographs taken parallel to the direction of sliding from a Stellite 6 disc sample which show the formation of a mechanically mixed nanolayer (red arrow) over an M_7C_3 carbide at the contacting surface following testing at 250 ^{o}C. (a) depicts a HAADF-STEM micrograph and (b) shows an accompanying Co map. (c) and (d) show higher magnification BF-TEM micrographs of this same carbide. 24

12 BF-STEM (a) and HAADF-STEM (b) micrographs taken parallel to the sliding direction from a Stellite 6 disc sample showing a $\sim$ 100 nm thick fractured M_7C_3 carbide in the nanocrystalline Co-rich matrix situated at the contacting surface following testing at 20 ^{o}C. 25

13 Schematic illustrating the different layers within the TAM used to describe the continuum of plastic deformation within the subsurface. The dashed line is a schematic representation of the extent of plastic flow within the subsurface (not to scale). The further right the line is, the greater the plastic deformation. 28

A-1 XRD pattern obtained from the polished surface of the as-received, HIPed Stellite 6. The ICDD database files used to index the diffractogram is shown in the legend. Stellite 6 exhibits reflections for γ-Co (fcc), M_7C_3 and a very small fraction of ϵ-Co (hcp). A-1

List of Tables

1 Chemical composition of HIPed Stellite 6 as determined by chemical analysis. 6

2 Phase fractions and crystallographic data of phases identified within HIPed Stellite 6 as determined via Rietveld analysis. 10

3 Summary of the dominant mechanisms governing the subsurface microstructural evolution beneath the contacting surface of Stellite 6 in response to sliding in lithiated water. 33

A-1 The effect of test temperature on the individual components of pin and disc mass loss of Stellite 6 following 5 h autoclave sliding contact testing with a dead load of 4 kg. The errors have been reported as the standard error of the mean. A-2